Environmental risks and strategies for long-term stability of carbon-based perovskite solar cells

Fanning Meng[1], Yi Zhou[1], Liguo Gao[1,*], Yang Li[1,*], Anmin Liu[1], Yanqiang Li[1], Chu Zhang[2], Meiqiang Fan[2], Guoying Wei[2], and Tingli Ma[2,3,*]

[1] State Key Laboratory of Fine Chemicals, Dalian University of Technology, Dalian, 116023, P. R. China.

[2] Department of Materials Science and Engineering, China Jiliang University, Hangzhou, 310018, P. R. China.

[3] Graduate School of Life Science and Systems Engineering, Kyushu Institute of Technology, Kitakyushu, Fukuoka 808-0196, Japan.

Corresponding Authors

*Liguo Gao

Tel: +86-427-2631810. E-mail: liguo.gao@dlut.edu.cn; ORCID: 0000-0002-5390-3663.

*Yang Li

E-mail: chyangli@dlut.edu.cn; ORCID: 0000-0002-5719-9044.

*Tingli Ma

Tel: 093-695-6045. E-mail: tinglima@life.kyutech.ac.jp; ORCID: 0000-0002-3310-459X.

Abstract

The decent power conversion efficiency (~20%), ultra-low cost and one-year stability make carbon-based perovskite solar cells (C-PSCs) one of the most promising candidates for commercialization in the field of perovskite photovoltaics. However, the stability of C-PSCs still lags behind that of the commercialized silicon and thin-film photovoltaics. Although there have been many reviews of the long-term stability of perovskite solar cells (PSCs), none has specifically focused on the long-term stability of C-PSCs. Herein, we summarize the environmental risks and strategies for ensuring the long-term stability of C-PSCs, highlighting also the various contributions of our research group. The most important factors affecting long-term stability are analyzed according to the environmental risks (i.e. moisture, oxygen, light, and thermal stress) of device degradation. The proposed strategies chiefly center around improving the intrinsic stability and strengthening encapsulation. In our conclusions, we also present an outlook on future work concerning stability improvements of C-PSCs. Our work provides a clear guideline for future research on C-PSCs.

Keyword: Carbon-based perovskite solar cells; Environmental risks and strategies; Perovskite solar cells; Stability

1. Introduction

To date, perovskite solar cells (PSCs) have achieved a certified power conversion efficiency (PCE) of 25.2% [1] due to their excellent optical and electronic properties such as an excellent light absorption coefficient, high external quantum efficiency, and long carrier diffusion length [2-4]. However, two main issues have thus far precluded commercialization. One is the cost issue as a result of the utilization of noble metals (such as gold or silver) as back electrodes, which are expensive, rare, and energy-intensive. The other is the long-term stability issue that stems from the deterioration of charge transport materials and the degradation of perovskite (PVK) materials, including (1) rapid decomposition induced by water [5-7], (2) oxidation triggered by oxygen molecules and accelerated by light [8,9], (3) light-induced cation segregation and halide segregation [10], (4) nonphotoactive phase transformation induced by high temperature [11,12], and (5) reaction with the migrated metal ions generating metal halides [10,13,14]. To overcome these problems, several strategies have been proposed, including utilizing stable charge transport materials [15,16], performing composition engineering of PVK [17], and replacing noble metal electrodes with such alternatives as MXene [18], carbon [19], Al [20], Cu [21], and Ni [22], etc. Carbon materials have some distinct advantages, e.g. low cost, abundant sources, robust hydrophobicity as sealant to resist PVK decomposition induced by moisture, and high chemical stability to avoid PVK degradation induced by the migration of metal ions [19,23,24]. It is thus considered to be the most promising material for replacing noble metal electrodes [25-27]. To date, carbon-based PSCs (C-PSCs) have achieved a PCE of ~20% and one-year stability, exhibiting good durability and excellent long-term stability compared with their noble metal-based counterparts [28-31].

While there have been many investigations and reviews of the stability of PSCs [25,26,32-35], a comprehensive account of the stability of C-PSCs is conspicuously absent. Herein, we summarize the environmental risks and key strategies for

long-term stability of C-PSCs, as shown in Fig. 1. We also draw important conclusions and present an outlook to guide research efforts aiming at improving the long-term stability of C-PSCs.

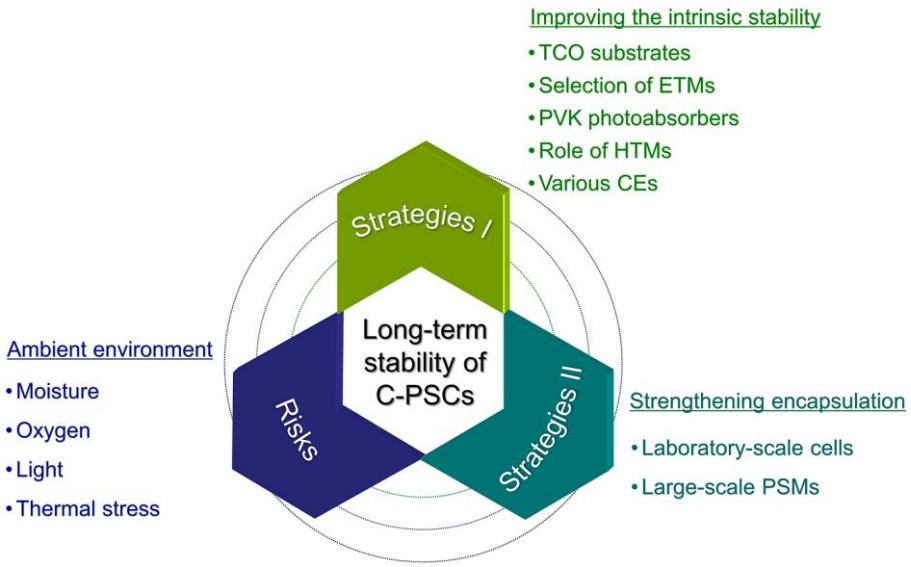

Fig.1 The summary of the environmental risks and strategies for long-term stable C-PSCs.

2. Environmental risks

During fabrication, storage, and operation, C-PSCs are inevitably influenced by the ambient environment. The instability of C-PSCs is primarily a result of the decomposition of PVK materials and the deterioration of charge transport materials. No matter whether encapsulated or not, degradation is linked closely to moisture, oxygen, light, thermal stress, and, importantly, their synergistic effects under atmospheric conditions. A brief overview of each factor is as follows:

(1) Moisture. Moisture can easily permeate into the bulk of PVK and produce PVK hydrate. The strong hydrogen bonds between water molecules and organic cations consequently weaken the chemical bond between the cation and PbX_6^- (X=I, Br, or Cl), resulting in rapid deprotonation of the organic cation and thus degradation of the PVK – especially in the presence of extrinsic stresses, e.g. thermal stress or electric fields [5-7]. Furthermore, the use of hygroscopic dopants in hole transport materials (HTMs) can also induce moisture degradation of PVK [36-38].

(2) Oxygen. Oxygen can oxidize both metal oxide charge transport materials

(especially TiO_2) and PVK photoabsorbers, causing a drop in the performance of PSCs. TiO_2 is notorious for readily combining with atmospheric oxygen, in turn generating superoxides (i.e. O_2^-) particularly under ultraviolet (UV) irradiation. These superoxides subsequently participate the oxidative decomposition of PVK [39,40]. The direct effect of oxygen on PVK is due to the formation of peroxides or superoxides as well, which can react with the organic cation (i.e., MA^+) and thus quicken the decomposition of PVK [39]. In particular, the combined effect of light and oxygen can lead to the decomposition of $MAPbI_3$ PVK, generating PbI_2, I_2, H_2O, and gaseous CH_3NH_2 [8,9].

(3) Light. Besides the synergistic decomposition of light and oxygen, light-induced decomposition of $MAPbI_3$ can occur even in the absence of oxygen. Under light illumination, when photons receive much higher energy than the bandgap of PVK compounds, electrons in the valence band are excited by such high-energy photons (approximately >3 eV) can antibond orbitals of NH_3 [41]. As a result, the N–H bonds in MA^+ can become dissociated and form gaseous CH_3NH_2 as well as H_2. In addition, excess carriers in PVK and the capture of photogenerated electrons in the conduction band can accelerate these chemical reactions in the presence of oxygen. Besides the chemical reactions, light-induced cation segregation and halide segregation can also significantly reduce the stability of PVK materials [10].

(4) Thermal stress. The thermal degradation of C-PSCs can be attributed to the following three reasons. First, the low thermal conductivity of PVK materials precludes rapid transfer of heat to the surrounding environment when experiencing high temperatures. Excessive heat accumulation results in significant thermal stress, which typically leads to the degradation or nonphotoactive phase transformation of PVK [12,42]. This problem is exacerbated when thick carbon layers ($\geqslant$10 μm) are used as back electrodes [43]. Second, the chemical reaction between MA^+ cations of PVK and carbon atoms of carbon layers can degrade the PVK photoabsorbers [44]. Third, some organic HTMs are unstable and are prone to high-temperature decomposition, e.g. 2,2',7,7'-Tetrakis[N,N-di(4-methoxyphenyl)amino]-9,9'-spirobifluorene

(spiro-OMeTAD), resulting in performance deterioration of the devices [45].

Generally, while the degradation of C-PSCs during operation is multifactorial, device resistance to light- and thermal-induced decomposition essentially depends on the intrinsic stability of functional materials [46,47]. In contrast, device resistance to moisture- and oxygen-induced decomposition depends more on the encapsulation techniques in addition to the intrinsic properties of the materials [48,49]. To minimize the environmental risks (i.e. moisture, oxygen, light, and thermal stress) that can cause device degradation, strategies for improving the long-term stability of C-PSCs can thus be divided into two distinct categories: (1) improving the intrinsic stability, and (2) strengthening encapsulation. Below, these two strategies are summarized.

3. Improving intrinsic stability

To improve the long-term stability of C-PSCs, one of the most important strategies is to enhance the intrinsic stability of the relevant components. Using stable materials can not only significantly reduce the risk of device decomposition, thus extending lifespan, but also bring down the cost of device encapsulation. Generally, C-PSCs consist of transparent conductive oxide (TCO) substrate/electron transport material (ETM)/PVK photoabsorber/carbon electrode (CE). In some cases, HTMs are incorporated into the device structure. Depending on whether HTMs are utilized, C-PSCs are classified as either HTM-free C-PSCs or HTM-based C-PSCs. Furthermore, based on the deposition process of the functional layers, C-PSCs are classified as having either a monolithic structure or a layer-by-layer structure. Consequently, C-PSCs have evolved into four types: HTM-free C-PSCs with a monolithic structure; HTM-based C-PSCs with a monolithic structure; HTM-free C-PSCs with a layer-by-layer structure; and HTM-based C-PSCs with a layer-by-layer structure, as shown in Fig. 2a-d. When there is no mesoporous TiO_2 (m-TiO_2) in the layer-by-layer structure, C-PSCs form a planar structure. The effects of the intrinsic properties of materials on the long-term stability of differently-structured devices are summarized below.

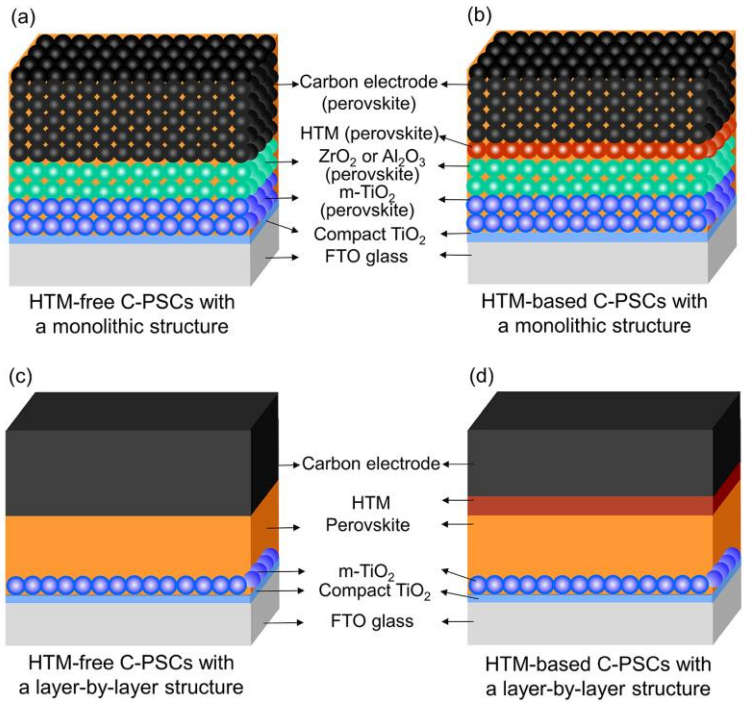

Fig.2 Device structure schematics of C-PSCs using TiO_2 as ETM: (a) HTM-free C-PSCs with a monolithic structure; (b) HTM-based C-PSCs with a monolithic structure; (c) HTM-free C-PSCs with a layer-by layer structure; and (d) HTM-based C-PSCs with a layer-by-layer structure.

3.1 TCO substrates

The commonly used TCO glass substrates for PSCs include indium-doped tin oxide (ITO) glass and fluorine-doped tin oxide (FTO) glass [50,51]. Since TCO glass substrates have excellent mechanical, chemical, and thermal stability, negative effects on the stability of devices are negligible. However, in the case of C-PSCs, substrate selection must take special factors into consideration. Generally, ITO glass exhibits higher transmittance in the visible light range, as well as higher conductivity and lower surface roughness than FTO glass. High-efficiency and planar C-PSCs are thus more likely to use ITO glass substrate. For example, Zhou et al. fabricated planar structure C-PSCs using ITO glass substrate [52]. The PCE of the resultant device exceeded 16%. Meanwhile, the device without encapsulation retained 80% of its initial PCE after a maximum power point (MPP) tracking of 505 h in ambient air. Compared to ITO glass, however, FTO glass is cheaper and has greater resistance to high temperatures and pressure. Since the cost of FTO glass is lower, it is more frequently used as substrate than ITO glass [32,53]. More pertinently, FTO glass is

more suitable than ITO glass given the high temperature sintering during ETM fabrication and the mechanical pressure of CE deposition [30,54,55]. Wei et al. hot-pressed a flexible carbon film on FTO/TiO_2/PVK substrate under 0.25 MPa pressure, with the resultant device achieving a PCE of 13.53% [54]. After storage for 20 d in air, the PCE of the device without encapsulation dropped only by 5%. Our group reported the fabrication of Coal-based CE by hot-pressing the carbon layer on FTO/TiO_2/PVK substrate under 0.4 MPa pressure [55]. Zhang et al. press-transferred a self-adhesive carbon film on FTO/TiO_2/PVK substrate under 0.7 MPa pressure [30]. The PCE of the champion device reached 19.2% and retained 94% of its initial value after an MPP tracking of 80 h under a N_2 atmosphere. The long-term stability profiles of the relevant C-PSCs are shown in Table 1.

Table 1 The long-term stability profiles of relevant C-PSCs using ITO or FTO glass substrates.

No.	Device structures	Champion PCE (%)	Pressure (MPa)	Encapsulation	Testing environments	Time scale	Remaining value of the initial PCE	Ref.
1	ITO/HMB:C_{60}/$MAPbI_3$ /Carbon	16.03	–	W/O	Air; 1 sun illumination (UV filter); MPP tracking; RT; 20%~30% RH	505 h	80%	[52]
2	FTO/c-TiO_2/m-TiO_2/$MAPbI_3$/Carbon	13.53	0.25	W/O	Air; RT	20 d	95.1%	[54]
3	FTO/c-TiO_2/m-TiO_2/ $Cs_{0.05}(MA_{0.17}FA_{0.83})_{0.95}Pb(I_{0.83}Br_{0.17})_3$ /Carbon	10.87	0.4	W/O	Air; dark condition; RT; 30% RH	120 h	84.4%	[55]
4	FTO/c-TiO_2/m-TiO_2/ $FA_yMA_{1-y}PbI_{3-x}Br_x$ /spiro-OMeTAD/Carbon	19.2	0.7	W/O	N_2; AM 1.5 sun-equivalent light intensity (UV-free white LED); MPP tracking; 20°C	80 h	94%	[30]

Notes

c-TiO_2, compact layer TiO_2;

HMB:C_{60}, hexamethonium bromide (HMB)-doped fullerene;

MA^+, $CH_3NH_3^+$;

FA^+, $NH_2CH{=}NH_2^+$;

RH, relative humidity;

RT, room temperature;

W, with;

W/O, without;

LED, light-emitting diode.

3.2 Selection of ETMs

A suitable ETM for highly-efficient and long-term stable C-PSCs should fulfill the following criteria: (1) high visible light transmittance to increase the light harvesting efficiency of the PVK photoabsorbers; (2) high electron mobility to achieve effective electron extraction and transfer at the ETM/PVK interface; and (3) good UV stability to reduce the oxidative decomposition of PVK [15,16]. To date, the reported ETMs for C-PSCs contain TiO_2, fullerene (C_{60}), ZnO, SnO_2 and Nb_2O_5. The effects of ETMs on the stability of differently-structured devices are summarized below.

3.2.1 ETMs for monolithic structures

Due to its excellent chemical stability and high light transmittance in the visible light spectrum [56-58], TiO_2 is widely used as ETM in C-PSCs. For monolithic structures, m-TiO_2 has the dual function of acting as mesoporous scaffold and ETM, as shown in Fig. 2a-b. Thus, it is indispensable in C-PSCs with a monolithic structure. Because the thickness of m-TiO_2 can significantly influence the depletion width at the ETM/PVK interface, it is usually thicker in HTM-free C-PSCs with a monolithic structure (usually ~1 μm).

In 2013, Ku et al. first reported on monolithic C-PSCs [19]. The triple mesoporous scaffold consisted of 1 μm m-TiO_2, 1 μm m-ZrO_2, and 10 μm mesoporous CE, which were printed layer by layer. Finally, the $CH_3NH_3PbI_3$ ($MAPbI_3$) PVK precursor was drop-casted on the top of the CEs and infiltrated in the triple mesoporous scaffold, as shown in Fig. 2a. This device achieved a PCE of 6.64%. After storage for 840 h under a dry air atmosphere in the dark, the devices without encapsulation suffered almost no decrease in PCE (Fig. 3a), exhibiting much better long-term stability than their Au electrode counterparts. Liu et al. prepared dual-sized TiO_2 nanoparticles as scaffold layers for monolithic structures and adjusted their thickness to 712 nm [59]. The device without encapsulation retained nearly 100% of its initial PCE for over 720 h in ambient air with ~45% relative humidity (RH).

Research on monolithic C-PSCs has been extensive since the first report was published in 2013. As a great deal of work on stability issues has mainly focused on PVK photoabsorbers, the relevant studies are summarized in section 3.3, PVK photoabsorbers.

3.2.2 ETMs for layer-by-layer structures

In C-PSCs with a layer-by-layer structure (Fig. 2c-d), the selection of ETMs is varied. Compact TiO_2 (c-TiO_2)/m-TiO_2 composites are commonly used, with the thickness of m-TiO_2 ranging from ~100 to ~600 nm. Although the presence of m-TiO_2 can boost the efficiency of the device, it is not essential [60]. For devices with a planar architecture, m-TiO_2 is not used and c-TiO_2 can be replaced with C_{60}, ZnO, SnO_2, or Nb_2O_5.

In 2014, our group reported C-PSCs based on a TiO_2/$MAPbI_3$ heterojunction, achieving a PCE of 9.08% [23]. The C-PSCs without any encapsulation kept their initial PCE for over 2000 h after storage under an air atmosphere in the dark, as shown in Fig. 3b. Zhang et al. optimized the thickness of the m-TiO_2 layer to 630 nm, as shown in Fig. 3c [61]. They achieved a PCE of 8.31%, and the device without encapsulation showed a slight increase in PCE after storage for 800 h in air. With m-TiO_2 nanoparticles, it is difficult to achieve a fast charge transport and thick PVK absorber layer simultaneously. Zheng et al. and Liu et al. designed TiO_2 ETMs with different structures for C-PSCs [62, 63]. The former came up with m-TiO_2 nanobowl (NB) arrays as ETMs, with the PCE of the device without encapsulation only dropping by 8% after storage for 45 d in air at room temperature (RT) and 10%~20% RH [62]. The latter synthesized Cs-doped TiO_2 nanorod (NR) arrays as ETMs [63], achieving a PCE of 9.5%. Importantly, the device without encapsulation showed no decline in performance after storage for 3000 h in ambient air. Even though TiO_2 is widely used as ETM in C-PSCs, it has certain disadvantages. First, it is instable when exposed to UV. The photocatalytic activity of TiO_2 is closely related to the oxygen vacancies on its surface. Under continuous UV illumination, oxygen molecules react with the surface oxygen vacancies on TiO_2, creating superoxides. Eventually, the

adjacent contact layer including PVK is oxidized and decomposed by the superoxides [39,40]. Second, TiO_2 has a low electron mobility (~1 $cm^2 \cdot V^{-1} \cdot s^{-1}$) compared to PVK materials (24.81 $cm^2 \cdot V^{-1} \cdot s^{-1}$) [64]. Third, TiO_2 has a high defect density [65]. Fourth, the fabrication of TiO_2 is highly energy consuming as it requires a high-temperature (~500°C) sintering step [66]. Therefore, to obtain highly efficient and highly stable C-PSCs with a layer-by-layer structure, it is essential to replace TiO_2 with materials characterized by high UV stability, low-temperature processability, and good electron mobility.

Compared with TiO_2, C_{60} boasts high electron mobility (1.6 $cm^2 \cdot V^{-1} \cdot s^{-1}$) [67] and high electron affinity [68]. And the C_{60}-based PSCs usually demonstrate a slighter hysteresis phenomenon and have excellent UV photostability [69,70]. These advantages make C_{60} an extremely promising alternative for TiO_2. Ahn et al. fabricated C-PSCs using C_{60} as ETM, and the resultant C_{60}-based devices exhibited superior stability compared to the TiO_2-based counterparts under continuous 100 $mW \cdot cm^{-2}$ illumination [71]. Meng et al. found that using C_{60} as ETM facilitated electron extraction, suppressed charge recombination, and reduced the sub-bandgap states at the C_{60}/$MAPbI_3$ interface [29]. A PCE of 15.38% was achieved in C_{60}-based devices. Meanwhile, the devices without any encapsulation retained 95% of their initial PCE after storage for 20 d in air with 40%~60% RH, as shown in Fig. 3d. And after an MPP tracking of 180 h in ambient atmosphere, the drop in PCE was only 5%. Zhou et al. further utilized hexamethonium bromide (HMB)-doped C_{60} as ETM, achieving both a decent PCE (16.03%) and good stability [52]. The devices without any encapsulation maintained 80% of their initial PCE after an MPP tracking of 505 h in air. Although the use of C_{60} as ETM improves the stability of C-PSCs, there are still some important factors that limit the development of C_{60}-based devices, e.g. the scarcity of C_{60} resource, poor processability, high cost, and high energy consumption as a result of the vacuum thermal evaporation deposition process [72,73].

In addition to C_{60}, another viable alternative to TiO_2 is ZnO. Despite having similar physical properties as TiO_2, the electron mobility of ZnO is far superior

(205~300 $cm^2 \cdot V^{-1} \cdot s^{-1}$) [74]. In addition, ZnO can be deposited by spin-coating and annealed at low temperature (<150°C) [75,76]. In 2015, our group for the first time reported C-PSCs that used ZnO as ETM, achieving a PCE of 8.07% [77]. Unfortunately, the ZnO-based devices suffered from poor stability (500 min in air), which were attributed to the high-density defects at the ZnO/PVK interface. To solve this problem, Shirazi et al. devised a composite ZnO/Al-doped ZnO layer [78]. Although this did not significantly improve the PCE of the device (8.23%), it made a big difference with regards to long-term stability. After storage for 15 d in ambient air without encapsulation, the PCE of the device retained 95.3% of its initial value. Yang et al. also used ZnO as ETM, obtaining C-PSCs of greater stability [79]. The champion device without encapsulation kept >90% of its initial PCE after storage for 1200 h in ambient air with 25~28ºC and 45%~60% RH.

SnO_2 is also considered as a suitable ETM for PSCs due to the following valuable characteristics: (1) wide optical bandgap (3.6~4.0 eV); (2) high visible light transmittance; (3) good UV photostability; (4) high electron mobility (~200 $cm^2 \cdot V^{-1} \cdot s^{-1}$), which is two orders of magnitude faster than that of TiO_2; and (5) low-temperature processability [16]. Lin et al. fabricated highly-stable planar C-PSCs based on SnO_2 ETM [80]. The performance of the device did not deteriorate after storage for 150 d in ambient atmosphere (Fig. 3e). Qiang et al. optimized the thickness of the SnO_2 layer to boost stability [81]. Doping SnO_2 with metal aliovalent cations is an effective approach to enhance the electron extraction and transfer at the ETM/PVK interface [82]. Ye et al., for instance, used Zn-doped SnO_2 as ETM, resulting in planar C-PSCs with a PCE of 17.78% [83]. The devices without encapsulation maintained nearly 100% of their initial PCE after storage for 1200 h in air. Moreover, to reduce the loss of open-circuit voltage (V_{oc}) at the SnO_2/PVK interface, our group used a $SnCl_2$ solution to passivate the SnO_2 layer and thereby produced a high V_{oc} (1.31 V) device [84]. The passivated device without encapsulation kept 95.5% of its initial PCE after heating at 90°C for 80 h in air with 60%~70% RH.

As an n-type semiconductor, Nb_2O_5 has a wide optical band gap (>3 eV) and high electron mobility [85,86]. Zhao et al. fabricated all-inorganic C-PSCs using a novel amorphous Nb_2O_5 (a-Nb_2O_5) as ETM, as shown in Fig. 3f [87]. This greatly increased the stability of the a-Nb_2O_5-based device, which retained nearly 100% of its initial PCE after storage for 60 d in air. The long-term stability profiles of layer-by-layer C-PSCs using different ETMs are shown in Table 2.

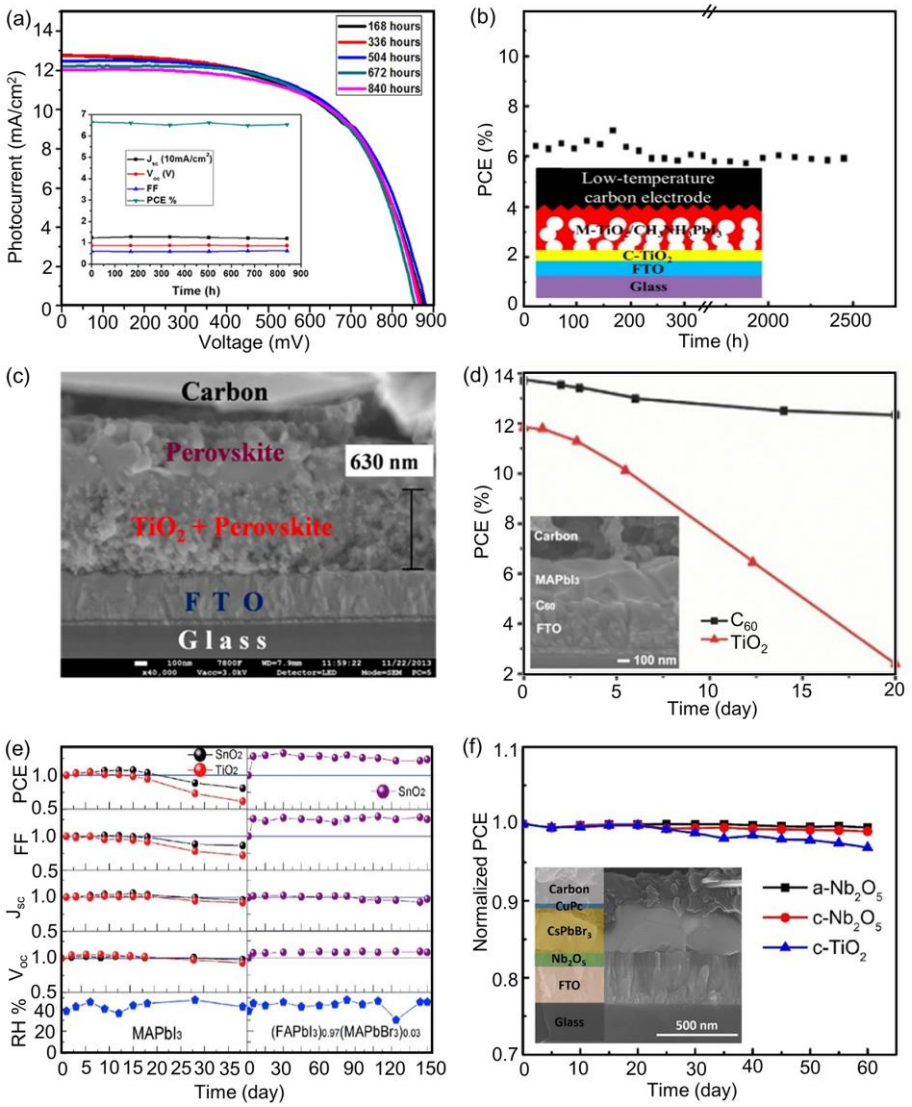

Fig.3 (a) Long-term stability of the C-PSCs without encapsulation using TiO_2 as ETM at RT in the dark; the inset is the changing parameter characters of the device within 840 h after been fabricated [19]. Reproduced from ref. 19 with permission. (b) Long-term stability of the devices based on TiO_2/$MAPbI_3$ heterojunction without encapsulation under an air atmosphere in the dark; the inset is corresponding device structure [23]. Reproduced from ref. 23 with permission. (c) The

cross-sectional scanning electron microscopy (SEM) images of the C-PSCs with optimal thickness of TiO_2 630 nm [61]. Reproduced from ref. 61 with permission. (d) Long-term stability test of the C-PSCs based on C_{60} and TiO_2 ETMs without encapsulation in ambient air with 40–60% RH at RT; the inset is the cross-sectional SEM image of C_{60}-based device [29]. Reproduced from ref. 29 with permission. (e) Long-term stability of the unencapsulated C-PSCs using SnO_2 or TiO_2 as ETMs and using $MAPbI_3$ (left) or $(FAPbI_3)_{0.97}(MAPbBr_3)_{0.03}$ (right) as perovskite materials in the dark [80]. Reproduced from ref. 80 with permission. (f) Long-term stability of C-PSCs based on a-Nb_2O_5, crystalline Nb_2O_5 (c-Nb_2O_5) and c-TiO_2 ETMs without encapsulation in air with ~40% RH at 25°C for 60 d, the inset is the cross-sectional SEM image of the whole device [87]. Reproduced from ref. 87 with permission.

Table 2 The long-term stability profiles of layer-by-layer C-PSCs using different ETMs.

No.	Device structures	Champion PCE (%)	Encapsulation	Testing environments	Time scale	Remaining value of the initial PCE	Ref.
1	FTO/c-TiO_2/m-TiO_2/$MAPbI_3$/Carbon	9.08	W/O	Air; dark condition	>2000 h	100%	[23]
2	FTO/c-TiO_2/m-TiO_2/$MAPbI_3$/Carbon	8.31	W/O	Air; RT	800 h	100%	[61]
3	FTO/c-TiO_2/NB-TiO_2/$MAPbI_3$/Carbon	12.02	W/O	Air; RT; 10%~20% RH	45 d	92.2%	[62]
4	FTO/c-TiO_2/NR-Cs:TiO_2/$CsPbI_3$/Carbon	9.5	W/O	Air; 20~30°C; 20%~30% RH	3000 h	100%	[63]
5	FTO/C_{60}/$MAPbI_3$/Carbon	15.38	W/O	Air; RT; 40%~60% RH	20 d	95%	[29]
			W/O	Air; 1 sun illumination (UV filter); MPP tracking; 40%~60% RH	180 h	95%	[29]
6	ITO/HMB:C_{60}/$MAPbI_3$/Carbon	16.03	W/O	Air; RT; 20%~30% RH	>60 d	81.9%	[52]
			W/O	Air; 1 sun illumination (UV filter); MPP tracking; RT; 20%~30% RH	505 h	80%	[52]
7	PEN/ITO/ZnO/$MAPbI_3$/Carbon	8.07	W/O	Air; dark condition; RT	8.33 h	80%	[77]
8	FTO/ZnO/AZO/$MAPbI_3$/Carbon	8.23	W/O	Air; RT	15 d	95.3%	[78]
9	FTO/ZnO/$MAPbI_3$/Carbon	13.62	W/O	Air; 25~28°C; 45%~60% RH	1200 h	>90%	[79]
10	FTO/SnO_2/$(FAPbI_3)_{0.97}(MAPbBr_3)_{0.03}$/Carbon	14.5	W/O	Air; RT; 45％ RH	150 d	100%	[80]
11	FTO/SnO_2/$MAPbI_3$/Carbon	8.32	W/O	Air; dark condition; 25°C; 20% RH	32 d	~92%	[81]

No.	Device structures	Champion PCE (%)	Encapsulation	Testing environments	Time scale	Remaining value of the initial PCE	Ref.
12	FTO/Zn:SnO_2/$Cs_{0.05}FA_{0.79}MA_{0.16}PbI_{2.5}Br_{0.5}$/CuPc/Carbon	17.78	W/O	Air; 20% RH	1200 h	100%	[83]
13	ITO/SnO_2/$CsPbIBr_2$/Carbon	7.00	W/O	Air; 90°C; 60%~70% RH	80 h	95.5%	[84]
14	FTO/a-Nb_2O_5/$CsPbBr_3$/CuPc/Carbon	5.74	W/O	Air; 25°C; 40% RH	60 d	99.5%	[87]

Notes

AZO, Al-doped ZnO;

CuPc, Copper(II) Phthalocyanine.

3.3 PVK photoabsorbers

In both monolithic and layer-by-layer structures, the instability of the devices can largely be attributed to the degradation of PVK materials. PVK materials have many shortcomings with regards to stability-related issues: (1) they easily dissolve in water, and frequently suffer from oxidative decomposition [5,6,8,9]; and (2) the weak bonds within PVK compounds or feeble interactions with the adjacent contact layers can be broken under continuous illumination and/or thermal stress [10-12]. To tackle these issues, composition engineering has emerged as a key strategy – a composite of various approaches such as the incorporation of mixed cations and/or mixed halides, the application of mixed-dimensional PVK, and the utilization of all-inorganic PVK [17]. Composition engineering can effectively tune the optoelectronic properties, improve the crystallinity and morphology, and enhance the intrinsic stability of PVK. For C-PSCs with a monolithic structure, in particular, the penetration of the PVK precursor is crucial since the precursor needs to pass through the micron-thick mesoscopic layers to make contact with TiO_2 [88]. As for C-PSCs with a layer-by-layer structure, PVK often encounters a large amount of corrosive solvent from carbon paste or wet carbon film [23,89], requiring highly-stable PVK films. The effects of PVK photoabsorbers on the stability of differently-structured devices are summarized below.

3.3.1 PVK for monolithic structures

For monolithic structures, the purpose of composition engineering is to tune the optoelectronic properties, improve the crystallinity and morphology, facilitate the penetration, and enhance the intrinsic stability of the PVK photoabsorbers [88,90,91]. Composition engineering related to stability issues includes the following PVK materials: $MAPbI_3$, $(5\text{-}AVA)_x(MA)_{1-x}PbI_3$ ($5\text{-}AVA^+$ = 5-aminovaleric acid cation), $PEA_xMA_{1-x}PbI_3$ (PEA^+ = phenethylammonium cation), $(5\text{-}AVA)_x(PEAI)_x(MA)_{1-x}PbI_{3+x}$, $FA_xMA_{1-x}PbI_3$ (FA^+ = formamidinium cation), $MAPb(I_{1-x}Br_x)_3$, $MAPbI_3(SrCl_2)_{0.1}$, and $Cs_{0.05}(FA_{0.4}MA_{0.6})_{0.95}PbI_{2.8}Br_{0.2}$.

In early PSCs, $MAPbI_3$ was the most commonly used PVK photoabsorber. Ku et al. reported the first monolithic C-PSC using $MAPbI_3$ as PVK photoabsorber [19]. However, incomplete infiltration of PVK crystals into the ZrO_2/TiO_2 mesoporous layer was responsible for a substantial amount of voids, resulting in a low PCE of 6.64% and just 840 h of stability in the dark.

To solve the penetration issue of the PVK precursor, a large number of systematic investigations have been carried out. Han et al. systematically studied the effects of CEs [92], insulating layer [93], particle size of TiO_2 [94], solvents in precursor [95], functional additives [96,97], and composition engineering [98], etc. Significantly, Rong et al. employed NH_4Cl as an additive in the PVK precursor, showing that the synergy effect of NH_4Cl in unison with a carefully controlled atmospheric humidity could effectuate the favorable transformation of PVK crystals in C-PSCs [97]. The champion device achieved a PCE of 15.6%, and it retained 96.7% of the initial PCE for over 130 d in ambient air. Mei et al. first synthesized a novel mixed cation PVK $(5\text{-}AVA)_x(MA)_{1-x}PbI_3$ by partially replacing MA^+ with $5\text{-}AVA^+$ [88]. The introduction of $5\text{-}AVA^+$ enhanced the penetration of the precursor, produced better pore filling in the triple mesoporous scaffold, and improved the crystallinity and morphology of PVK crystals, resulting in a longer exciton lifetime and a higher quantum yield for photoinduced charge separation. The champion device achieved a certified PCE of 12.8% and showed no degradation after exposure for >1000 h in ambient air under full sunlight.

Since the addition of $5\text{-}AVA^+$ to $MAPbI_3$ can bring about better penetration, improve the crystallinity and morphology, and enhance the intrinsic stability, much work has been done on this promising approach. The relevant findings are summarized according to the following categories: (1) stability of laboratory-scale cells in different test environments; (2) stability of large-scale carbon-based perovskite solar modules (PSMs); (3) stability improvement mechanism.

First, in laboratory-scale cells, Li et al. investigated the stability of $(5\text{-}AVA)_x(MA)_{1-x}PbI_3$ based C-PSCs in different test environments [99]. The devices

showed no significant drop in performance regardless of the test environments, including a hot desert climate, high-temperature (80~85°C) atmosphere, and continuous illumination, as shown in Fig. 4a-c. These impressive results indicate a promising future for the large-scale application of $(5\text{-AVA})_x(MA)_{1-x}PbI_3$ based C-PSCs.

Second, Hu et al. fabricated large-scale carbon-based PSMs using $(5\text{-AVA})_x(MA)_{1-x}PbI_3$ as the PVK photoabsorber [91], achieving a PCE of 10.4% for the 10×10 cm^2 module. Significantly, the PSMs showed no decline in performance under continuous light illumination for 1000 h in air, reached a lifespan of over 1 year in the dark, and suffered no degradation for a month in the local outdoor environment (~30°C, ~80% RH). Subsequently, a module with an active area of 7 m^2 was fabricated to test large-scale potential, as shown in Fig. 4d. In a separate study, Grancini et al. fabricated a one-year stable PSM by using an ultra-stable 2D/3D $(5\text{-AVA})_2PbI_4/MAPbI_3$ heterojunction [31]. This was because the wide bandgap 2D PVK layer (Fig. 4e-f) suppressed charge recombination at the 3D PVK and CE interface. The champion module achieved a PCE of 11.2% (substrate area: 10×10 cm^2) and a lifespan of over 10,000 h under continuous 100 $mW \cdot cm^{-2}$ illumination at 55°C, as shown in Fig. 4g. This 2D/3D $(5\text{-AVA})_2PbI_4/MAPbI_3$ heterojunction not only boosted the stability of 3D PVK but also facilitated excellent charge separation between 3D PVK and CEs, paving the way for the fabrication of highly efficient and ultra-stable PSMs.

Third, while numerous experimental results have confirmed that incorporating 5-AVA^+ into the PVK precursor solution can improve the stability of C-PSCs, the exact mechanism has yet to be ascertained. Hashmi et al. found that 5-AVA^+ decreases the crystallization rate of the PVK precursor, and that vacuum curing of the PVK could further promote crystal growth [100]. Pockett et al. substantiated that the anchor effect of 5-AVA^+ inhibits ion migration, which is likely related to the improved stability of the device [101]. Lin et al. observed that the 5-AVA^+ located at the grain surface of $MAPbI_3$ passivates surface defects, acting as a barrier that protects $MAPbI_3$

from oxidative degradation [102]. Péan et al. investigated the mechanism by which the oxidative degradation of $MAPbI_3$ and $(5\text{-}AVA)_xMA_{1-x}PbI_3$ occurs [90]. They revealed that the stability improvement of $(5\text{-}AVA)_xMA_{1-x}PbI_3$ was closely linked to the smaller grain size, lower defect concentration, denser morphology, less diffusion of oxygen molecules, and their combined effects.

In addition to $(5\text{-}AVA)_x(MA)_{1-x}PbI_3$, Xu et al. successfully introduced PEA^+ into $MAPbI_3$ and thus synthesized $PEA_xMA_{1-x}PbI_3$ PVK [103]. The device without encapsulation retained 90% of its initial PCE for over 80 d in air. Papadatos et al. further developed $(5\text{-}AVA)_x(PEAI)_x(MA)_{1-x}PbI_{3+x}$ PVK for monolithic structures [104]. Fu et al. fabricated FA_xMA_{1-x} PbI_3 and $MAPb(I_{1-x}Br_x)_3$ PVK for monolithic structures, with the resultant devices showing good environmental stability [105,106]. Zhang et al. fabricated $MAPbI_3(SrCl_2)_{0.1}$ PVK using a novel and eco-friendly $SrCl_2$ as an inorganic source for the precursor [107]. Since $MAPbI_3(SrCl_2)_{0.1}$ PVK had lower defect density and better penetration performance, the device achieved a PCE of 15.9%. Due to the positive effect of $SrCl_2$ on lattice stability, the device without encapsulation retained ~90% of its initial PCE for 1000 h under continuous illumination in ambient air. For monolithic C-PSCs, the photogenerated holes have to pass a relatively long way before effective collection by CEs. This makes it essential for PVK photosensitizers to increase the photogenerated carrier lifetime and diffusion length. To achieve this, Liu et al. first synthesized $Cs_{0.05}(FA_{0.4}MA_{0.6})_{0.95}PbI_{2.8}Br_{0.2}$ PVK, obtaining a device that achieved a PCE of 17.02% [108]. Since the introduction of Cs^+ reduces the effective radius of cations and suppresses the halide segregation, the inherent stability of the mixed PVK is significantly enhanced. The encapsulated device maintained 91% of its initial PCE after storage for 1020 h at 85°C and 40%~60% RH in the dark. The reported composition engineering of PVK is shown in Fig. 4h. The long-term stability profiles of monolithic C-PSCs using different PVK photoabsorbers are shown in Table 3.

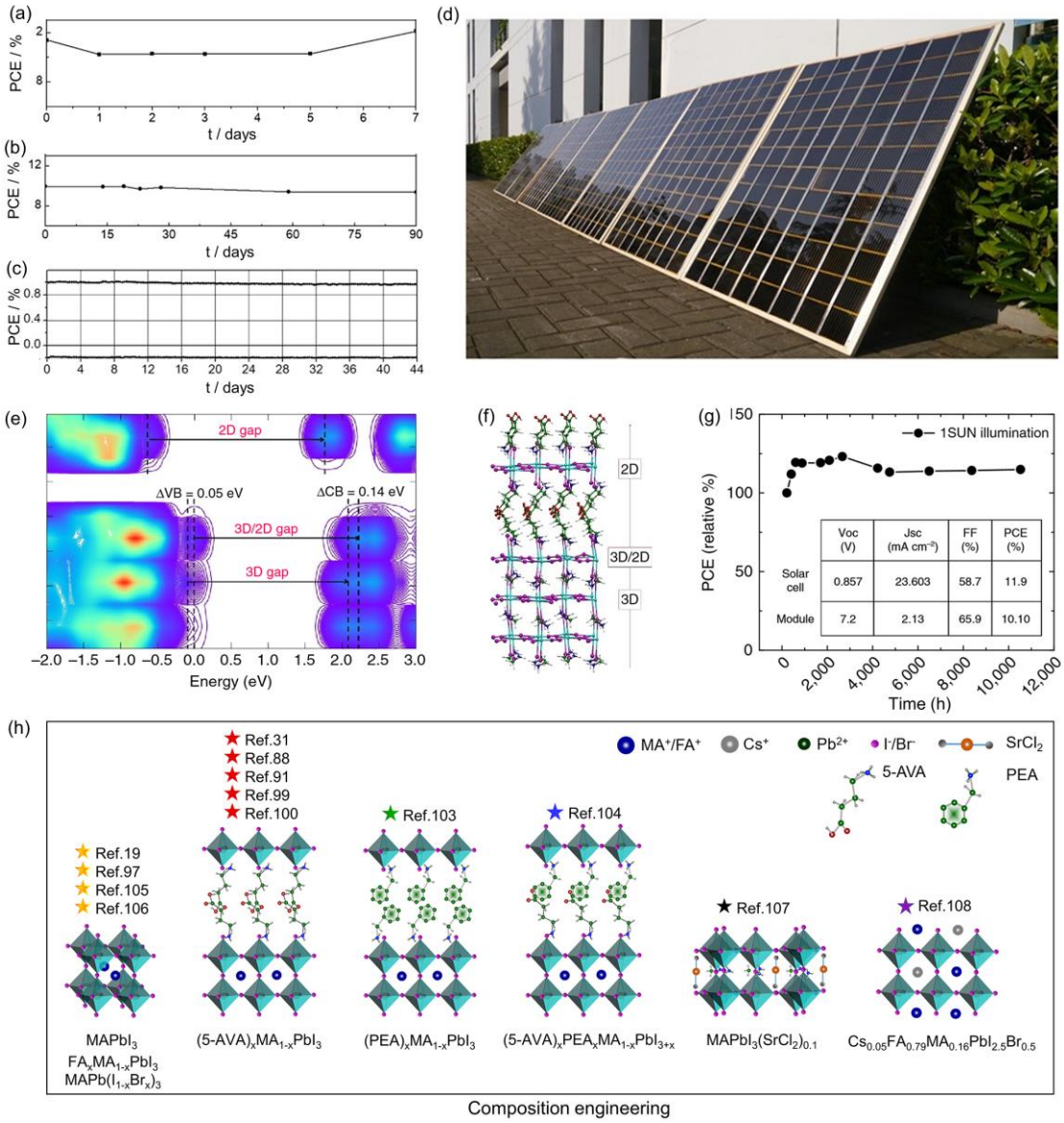

Fig.4 (a) PCE evolution of the encapsulated C-PSCs during outdoor stability testing in hot desert climate. (b) Indoor thermal stress test of C-PSCs which was encapsulated and kept for 3 months in a normal oven filled with ambient air at 80~85°C. (c) PCE evolution of C-PSCs under a Ar atmosphere with 45 °C and at MPP [99]. Reproduced from ref. 99 with permission. (d) Image of 7 m^2 carbon-based PSM [91]. Reproduced from ref. 91 with permission. First principles simulations of the 2D/3D interface: (e) local density of state of the 3D/2D interface and (f) interface structure with the 2D phase contacting the TiO_2 surface. (g) Typical module stability test under 1 sun illumination at stabilized temperature of 55°C and at short circuit conditions [31]. Reproduced from ref. 31 with permission. (h) The composition engineering of PVK for monolithic C-PSCs.

Table 3 The long-term stability profiles of monolithic C-PSCs using different PVK photoabsorbers.

No.	Device structures	Champion PCE (%)	Encapsulation	Testing environments	Time scale	Remaining value of the initial PCE	Ref.
1	FTO/c-TiO_2/m-TiO_2/m-ZrO_2/Carbon ($MAPbI_3$)	6.64	W/O	Air; dark condition; RT	840 h	97.9%	[19]
2	FTO/c-TiO_2/m-TiO_2/m-ZrO_2/Carbon ($MAPbI_3$)	15.60	W/O	Air; RT; 30% RH	130 d	96.7%	[97]
3	FTO/c-TiO_2/m-TiO_2/m-ZrO_2/Carbon ($(5\text{-}AVA)_x(MA)_{1-x}PbI_3$)	12.84	W/O	Air; 100 $mW\cdot cm^{-2}$ illumination; RT	1008 h	100%	[88]
4	FTO/c-TiO_2/m-TiO_2/m-ZrO_2/Carbon ($(5\text{-}AVA)_x(MA)_{1-x}PbI_3$)	12.9	W	Hot dessert climate	168 h	100%	[99]
			W	Air; 80~85°C	3 months	100%	[99]
			W/O	Ar; 100 $mW\cdot cm^{-2}$ (white LED); MPP; 45°C	>1056 h.	100%	[99]
5	FTO/c-TiO_2/m-TiO_2/m-ZrO_2/Carbon ($(5\text{-}AVA)_x(MA)_{1-x}PbI_3$)	10.4	–	Air; AM1.5 illumination; MPP; 25°C; 54% RH	1000 h	100%	[91]
			W/O	Dark condition	>1 year	100%	[91]
			W	Outdoor; ~30°C; ~80% RH	1 month	100%	[91]
6	FTO/c-TiO_2/m-TiO_2/m-ZrO_2/Carbon ($(5\text{-}AVA)_2PbI_4/MAPbI_3$)	11.16	W	1 sun illumination (UV filter); short circuit; 55°C	>10000 h	100%	[31]

No.	Device structures	Champion PCE (%)	Encapsulation	Testing environments	Time scale	Remaining value of the initial PCE	Ref.
7	FTO/c-TiO_2/m-TiO_2/m-ZrO_2/Carbon ($((5\text{-}AVA)_x(MA)_{1-x}PbI_3$)	8.47	W/O	100 mW·cm^{-2} illumination (UV filter); open circuit; 35ºC	1046 h	95.5%	[100]
8	FTO/c-TiO_2/m-TiO_2/m-ZrO_2/Carbon ($PEA_xMA_{1-x}PbI_3$)	8.68	W/O	Air	>80 d	90%	[103]
9	FTO/c-TiO_2/m-TiO_2/m-ZrO_2/Carbon ($((5\text{-}AVA)_x(PEA)_x(MA)_{1-x}PbI_{3+x}$)	7.11	–	Air; 40%~60％ RH	35 d	80%	[104]
10	FTO/c-TiO_2/m-TiO_2/m-ZrO_2/Carbon ($FA_xMA_{1-x}PbI_3$)	9.53	W/O	Air; RT; 50％ RH	49 d	91%	[105]
11	FTO/c-TiO_2/m-TiO_2/m-ZrO_2/Carbon ($MAPb(I_{1-x}Br_x)_3$)	9.99	W/O	Air; RT; 50％ RH	56 d	96.2%	[106]
12	FTO/c-TiO_2/m-TiO_2/m-Al_2O_3/Carbon ($(MAPbI_3)(SrCl_2)_{0.1}$	15.9	W/O	Air; 10 mW·cm^{-2} illumination (white LED) 25~28°C; 30%~55% RH	1000 h	90%	[107]
13	FTO/c-TiO_2/m-TiO_2/m-Al_2O_3/NiO/Carbon ($Cs_{0.05}(FA_{0.4}\ MA_{0.6})_{0.95}PbI_{2.8}Br_{0.2}$)	17.02	W	Dark condition; 85°C; 40%~60％ RH	1000 h	91%	[108]

3.3.2 PVK for layer-by-layer structures

For layer-by-layer structures, composition engineering intends to optimize optoelectronic properties, generate the high-quality films, and improve the intrinsic stability of the PVK photoabsorbers [109-111]. Composition engineering related to stability issues includes the following PVK materials: $MAPbI_3$, $MAPbBr_3$, $MAPbI_3/MAPbI_xBr_{3-x}$, $FA_xMA_{1-x}PbI_yBr_{3-y}$, $Cs_{0.05}FA_{0.79}MA_{0.16}PbI_{2.5}Br_{0.5}$, $Cs_{0.2}FA_{0.8}PbI_{2.64}Br_{0.36}$, $CsPbIBr_2$, $CsPbI_3$ and $(EA)_2(MA)_5Pb_6I_{19}$ (EA^+=ethylammonium cation).

In the early development of C-PSCs, performance and stability greatly depended on the quality of the $MAPbX_3$ (X=I, Br, or Cl) film. Chen et al. prepared dense and uniform $MAPbI_3$ film via scalable electrodeposition (Fig.5a), with the resultant device achieving a PCE of 10.19% [109]. The device without encapsulation maintained 98% of its initial PCE after storage for 30 d in ambient atmosphere. They also prepared uniform, even, and smooth $MAPbBr_3$ film for thermally stable C-PSCs [111]. The device without encapsulation showed no decline in PCE after storage for 90 d in dry air with 25~30^{o}C and 10~20% RH, and retained ~90% of its initial PCE after storage for 15 d under thermal stress (air, 80^{o}C, and 50%~85% RH). Yang et al. adopted NH_4Cl as an additive to improve the quality of $MAPbI_3$ film, with the PCE of the resultant device reaching 13.26% [79]. After storage for 1200 h in ambient air, the device without encapsulation maintained 91.3% of its initial PCE. Liu et al. synthesized a $MAPbI_3/MAPbI_xBr_{3-x}$ PVK stacking layer using in-situ growth technology [112]. The PVK stacking layer effectively suppressed charge interfacial recombination and electron reverse transfer (Fig.5b), allowing for a PCE of 16.2%. The device without encapsulation kept ~85% of its initial PCE after storage for 55 d in dark ambient conditions, as shown in Fig, 5c.

Yet, the $MAPbX_3$ (X=I, Br) PVK compounds have a number of drawbacks, e.g. low efficiency, moisture and thermal instability, and light-induced trap-state formation [113,114]. Consequently, using PVK with mixed cations and/or halides has received much attention in order to optimize the optoelectronic properties and improve

intrinsic stability. Zhou et al. first fabricated a multi-walled carbon nanotube (MWCNT)-doped $FA_xMA_{1-x}PbI_yBr_{3-y}$ film in ambient air [115]. The device achieved a PCE of 16.25% (active area 0.08 cm^2) and a PCE of 12.34% (active area 1 cm^2). The C-PSCs without encapsulation maintained 82.5% of its initial PCE after storage for 500 h at an 85°C air environment, retained 94.9% of its initial PCE after an MPP tracking of 500 h in air, and kept 92.5% of its initial PCE in ambient atmosphere for 154 d (Fig. 5d). Ye et al. prepared C-PSCs using the triple cation $Cs_{0.05}FA_{0.79}MA_{0.16}PbI_{2.5}Br_{0.5}$ PVK, achieving a PCE of 17.78% [83]. The device without encapsulation showed no performance decay after storage for 1200 h in air. Li et al. fabricated C-PSCs using the same PVK compound [116]. The device without encapsulation suffered no obvious performance decline in ambient atmosphere (27°C, 60% RH) for over 1000 h, and retained over 80% of its initial efficiency for 500 h at 85°C in dry air. Furthermore, since the $Cs_yFA_{1-y}Pb(I_{1-x}Br_x)_3$ compound does not contain the volatile component MA^+, its thermal and moisture stability is considerably improved. Wu et al. synthesized a $Cs_{0.2}FA_{0.8}PbI_{2.64}Br_{0.36}$ PVK photoabsorber, with the corresponding device without any encapsulation maintaining 91% of its initial PCE for 192 h at 85℃ and 85% RH atmosphere in the dark [117]. Wang et al. prepared all-inorganic $CsPbIBr_2$ PVK for C-PSCs and achieved a PCE of 7.6% [118]. The device without encapsulation kept 90% of its initial PCE after storage for 624 h in air at RT and 10% RH, and retained 96% of its initial PCE after storage for 192 h in a dry (RH=0%) air atmosphere at 80℃. Xiang et al. fabricated natrium doped $CsPbI_3$, with the resultant device achieving a PCE of 10.7% [119]. The device without encapsulation suffered no observable performance decline after storage for 70 d in air.

A distinct strategy to strengthen the intrinsic stability of PVK is to introduce moisture-resistant 2D PVK components into 3D PVK compounds. Zhou et al. incorporated the short carbon-chain EA^+ into 3D $MAPbI_3$ to generate a 2D component, constructing a novel 2D/3D hybrid $(EA)_2(MA)_5Pb_6I_{19}$ PVK [120]. The resultant C-PSCs without any encapsulation exhibited excellent long-term stability, thermal stability and photostability. They retained 93% of the initial PCE for 2160 h in

ambient air (Fig. 5e), 80% of their initial PCE for over 100 h during continuous heating at 80ºC, and 92% of their initial PCE after an MPP tracking of over 300 h. The relevant composition engineering of PVK is shown in Fig. 5f. The long-term stability profiles of layer-by-layer C-PSCs using different PVK photoabsorbers are shown in Table 4.

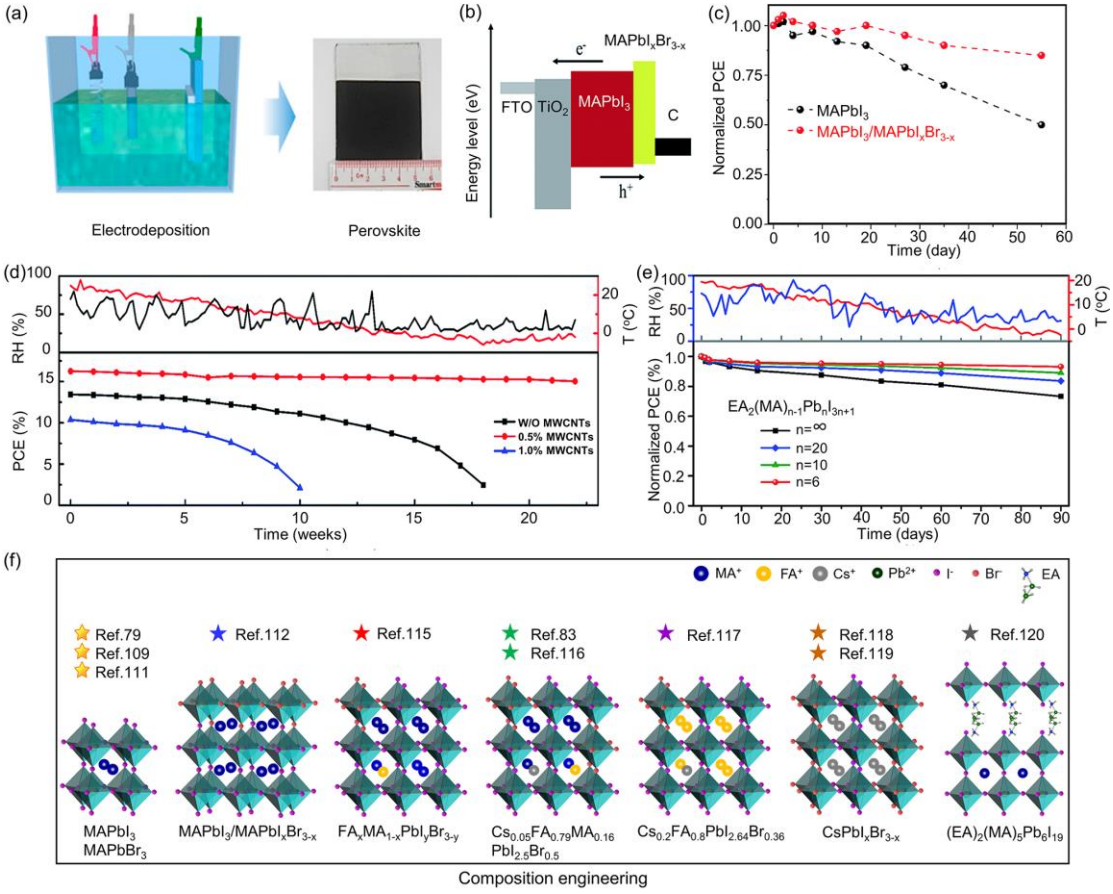

Fig.5 (a) Schematic illustration of the electrodepositing system and the prepared PVK film [109]. Reproduced from ref. 109 with permission. (b) Energy level diagram of the C-PSCs based on $MAPbI_3/MAPbI_xBr_{3-x}$. (c) PCE evolution of the $MAPbI_3$-based and $MAPbI_3/MAPbI_xBr_{3-x}$-based devices in dark ambient conditions (23°C, 30% RH) [112]. Reproduced from ref. 112 with permission. (d) PCE evolution of C-PSCs based on MWCNT doped PVK under monitored ambient conditions, including relative humidity (black curve, left axis) and the room temperature (red curve, right axis) [115]. Reproduced from ref. 115 with permission. (e) PCE evolution of the C-PSCs with $(EA)_2(MA)_{n-1}Pb_nI_{3n+1}$ under monitored ambient conditions, including relative humidity (blue curve, left axis) and the room temperature (red curve, right axis) [120]. Reproduced from ref. 120 with permission. (f) The composition engineering of PVK for

layer-by-layer C-PSCs.

Table 4 The long-term stability profiles of layer-by-layer C-PSCs using different PVK photoabsorbers.

No.	Device structures	Champion PCE (%)	Encapsulation	Testing environments	Time scale	Remaining value of the initial PCE	Ref.
1	FTO/c-TiO_2/m-TiO_2/$MAPbI_3$/Carbon	10.19	W/O	Air; ~25°C; 30% RH	30 d	98%	[109]
2	FTO/c-TiO_2/m-TiO_2/$MAPbBr_3$/Carbon	8.09	W/O	Air; 25~30°C; 10~20% RH	90 d	100%	[111]
			W/O	Air; 80°C; 50~85% RH	15 d	~90%	[111]
3	FTO/ZnO/$MAPbI_3$/Carbon	13.62	W/O	Air; 25~28°C; 45%~60% RH	1200 h	91.2%	[79]
4	FTO/c-TiO_2/m-TiO_2/ $MAPbI_3$:$MAPbI_xBr_{3-x}$/Carbon	16.2	W/O	Air; dark condition; 23°C; 30% RH	55 d	85%	[112]
5	ITO/SnO_2/MWCNTs: $FA_xMA_{1-x}PbI_y$ Br_{3-y}/Carbon	16.25	W/O	Air; 85°C	500 h	82.5%	[115]
			W/O	Air; 1 sun illumination; MPP tracking; 0~20°C; 30%~80% RH	500 h	94.9%	[115]
			W/O	Air; the monitored ambient RT and RH	154 d	92.5%	[115]
6	FTO/Zn:SnO_2/$Cs_{0.05}FA_{0.79}MA_{0.16}$ $PbI_{2.5}Br_{0.5}$/CuPc/Carbon	17.78	W/O	Air; 20% RH	1200 h	100%	[83]
7	FTO/c-TiO_2/m-TiO_2/$Cs_{0.05}FA_{0.79}MA_{0.16}$ $PbI_{2.5}Br_{0.5}$/Carbon	12.0	W/O	Air; 27°C; 60% RH	>1000 h	100%	[116]
			W/O	Air; 85°C	500 h	>80%	[116]
8	FTO/c-TiO_2/m-TiO_2/ $Cs_{0.2}FA_{0.8}PbI_{2.64}Br_{0.36}$/PEO/Carbon	14.5	W/O	Air; dark condition; 85°C; 85％RH	192 h	91%	[117]

No.	Device structures	Champion PCE (%)	Encapsulation	Testing environments	Time scale	Remaining value of the initial PCE	Ref.
9	FTO/ZnO/$CsPbIBr_2$/Carbon	7.60	W/O	Air; RT; 10% RH	624 h	91%	[118]
			W/O	Air; 80°C; 0% RH	192 h	96%	[118]
10	FTO/c-TiO_2/m-TiO_2/Na:$CsPbI_3$/Carbon	10.7	W/O	Air; 20~35°C; 10%~20% RH	70 d	100%	[119]
11	ITO/C_{60}/$(EA)_2(MA)_5Pb_6I_{19}$/Carbon	11.88	W/O	Air; the monitored ambient RT and RH	2160 h	93%	[120]
			W/O	Air; dark condition; 80°C	110 h	80%	[120]
			W/O	Air; 1 sun illumination (without UV filter); MPP tracking; 30%~80% RH	308 h	92%	[120]

Notes

PEO, polyethylene oxide;

EA^+, $CH_3CH_2NH_3^+$.

3.4 Role of HTMs

For C-PSCs, the advantageous role of HTMs is reflected in two aspects: (1) HTMs allow much more favorable energy level alignment between PVK and CEs, not only improving hole extraction and transfer but also suppressing the reverse transfer of electrons [26,121]. Therefore, if high efficiency is the goal, researchers are likely to prepare HTM-based C-PSCs. (2) Using hydrophobic, chemically-stable, and thermally-stable HTMs could provide extra protection for C-PSCs against degradation induced by environmental stress [71,122]. The effects of HTMs on the stability of differently-structured devices are summarized below.

3.4.1 HTMs for monolithic structures

For HTM-based C-PSCs with a monolithic structure, the HTM together with m-TiO_2，m-ZrO_2 and CE form the quadruple mesoscopic scaffold, as shown in Fig. 2b. HTMs are deposited by screen-printing the paste followed by sintering at high temperature (~500ºC) [123,124]. The particle size and thermal stability of HTMs are thus crucial. Due to its suitable particle size, good thermal stability, low cost, and wide bandgap, NiO has thus far proven to be an irreplaceable HTM for monolithic C-PSCs. Besides, spinel Co_3O_4 has also been shown to be an effective HTM, however, it has not attracted a lot research interest.

In 2015, Xu et al. reported the usage of NiO as HTM (Fig. 6a), with the resultant device achieving a PCE of 14.9% [123]. The device without encapsulation maintained over 93% of its initial PCE after storage for 1000 h in ambient atmosphere, and kept 80% of its initial PCE for >1000 h when exposed to an atmospheric temperature of 60ºC, as shown in Fig. 6b. However, the device without encapsulation lost about 80% of its initial PCE after light illumination for 150 h. Thereafter, Cao et al. used NiO as HTM for mesoscopic C-PSCs and attained a PCE of 15.03% [124]. The device without encapsulation exhibited ambient and thermal stability for 1000 h. Under continuous illumination, the encapsulated device kept over 75% of its initial PCE for 1000 h in air. Liu et al. similarly fabricated NiO-based devices and achieved an

impressive PCE of 17.02% [108]. The encapsulated device retained 91% of its initial PCE after storage for 1000 h at 85ºC and 40%~60％ RH atmosphere in dark conditions.

Although NiO has many advantages, the photovoltaic performance of NiO-based C-PSCs is not satisfying due to its high series resistance resulting from the low intrinsic conductivity of the NiO crystals [125,126]. Doping NiO with metal heteroatoms, e.g. Cu and Mg, decreases its valence band position, making for a larger potential difference between the hole and electron transport layers and fewer potential losses at the HTM/PVK interface [127,128]. Bashir et al. synthesized Cu-doped NiO for C-PSCs [129], as shown in Fig. 6c. The laboratory-scale cell and large-scale PSM (active area of 70 cm^2) achieved PCEs of 13.74% and 12.1%, respectively. The laboratory-scale cell without encapsulation retained ~90% of its initial PCE after storage for over 4500 h in air with 65% RH, as shown in Fig. 6d. No device degradation was observed after an MPP tracking of 60 h. Behrouznejad et al. utilized UV–O_3 treatment to increase the Ni^{3+} (Ni_2O_3) phase on the surface of the black NiO [130], achieving a PCE of 12.1%. The devices without encapsulation retained more than 80% of their initial PCE after storage for over 3 months in ambient air. As an irreplaceable HTM, the influence of UV and oxygen on the stability of NiO_x-based C-PSCs should be further studied due to the inherently photocatalytic activity of NiO_x [131,132]. Next, Jiang et al. compared the role of p-type metal oxides NiO, MoO_3, Co_2O_3, and CuO. They found that only the NiO-based devices showed performance enhancement [133]. Bashir et al. synthesized spinel Co_3O_4 nanomaterial as HTM (Fig. 6e), attaining a PCE of 13.27% [134]. Long-term stability of up to 2500 h in ambient air with 70% RH was achieved in devices without encapsulation, as shown in Fig. 6f. Further, the large-scale PSMs only lost <10% of their initial PCE under continuous light soaking for 140 h in air. The long-term stability profiles of C-PSCs using different HTMs are shown in Table 5.

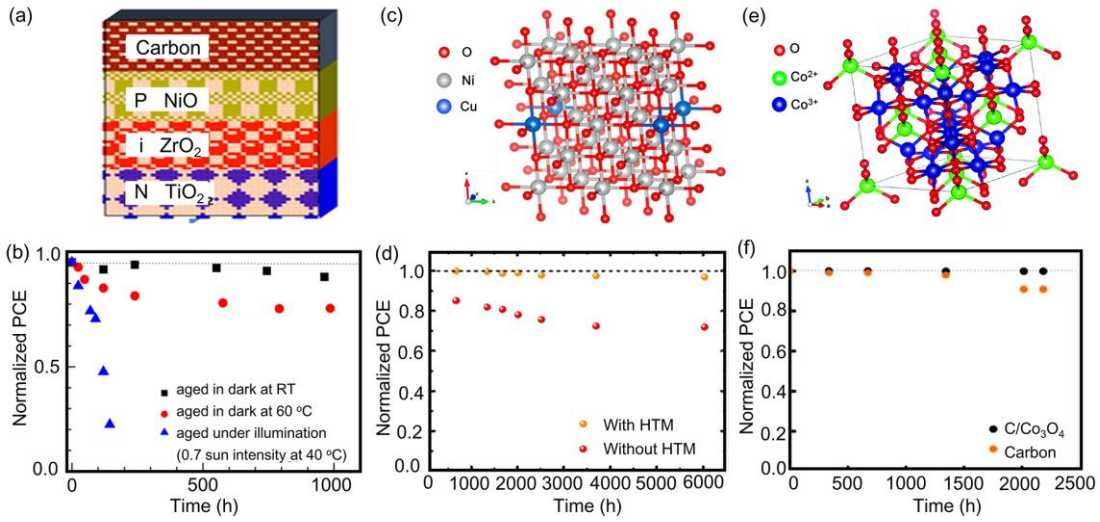

Fig.6 (a) Schematic of NiO-based C-PSCs with a monolithic structure. (b) PCE evolution of the C-PSCs under different test conditions, including storing at RT without light soaking (black), storing at 60°C without light soaking (red), and exposure to AM 1.5 simulated sunlight (0.7 sun) with a temperature at 45°C (blue) [123]. Reproduced from ref. 123 with permission. (c) Crystal structure of Cu:NiO. (d) PCE evolution of the C-PSCs with and without Cu:NiO HTM measured under ambient environment conditions [129]. Reproduced from ref. 129 with permission. (e) Crystal structure of Co_3O_4. (f) PCE evolution of the C-PSCs with and without Co_3O_4 HTM measured in ambient air [134]. Reproduced from ref. 134 with permission.

Table 5 The long-term stability profiles of monolithic structure C-PSCs using different HTMs.

No.	Device structures	Champion PCE (%)	Encapsulation	Testing environments	Time scale	Remaining value of the initial PCE	Ref.
1	FTO/c-TiO_2/m-TiO_2/m-ZrO_2/ NiO/Carbon ($MAPbI_3$)	14.9%	W/O	Air; dark condition; RT; ~40% RH	1000 h	＞93%	[123]
			W/O	Dark condition; 60°C; ~40% RH	>1000 h	80%	[123]
			W/O	0.7 full sun illumination; 45°C; ~40% RH	150 h	20%	[123]
2	FTO/c-TiO_2/m-TiO_2/m-Al_2O_3 /NiO/Carbon ($MAPbI_3$)	15.03	W/O	Air; dark condition; RT; ~40％ RH	1000 h	93.2%	[124]
			W/O	Dark condition; 60°C; ~10% RH	>1000 h	＞80%	[124]
			W	Air; light soaking (white LED) at 100 $mW \cdot cm^{-2}$ intensity; ~25°C; ~40％ RH	1000 h	＞75%	[124]
3	FTO/c-TiO_2/m-TiO_2/m-Al_2O_3 /NiO/Carbon ($Cs_{0.05}(FA_{0.4}\ MA_{0.6})_{0.95}PbI_{2.8}Br_{0.2}$)	17.02	W	Dark condition; 85°C; 40%~60％ RH	1000 h	91%	[108]
4	FTO/c-TiO_2/m-TiO_2/m-ZrO_2 /Cu:NiO/Carbon ($MAPbI_3$)	13.74	W/O	Air; 25°C; 65% RH	>4500 h	90%	[129]
5	FTO/c-TiO_2/m-TiO_2/m-Al_2O_3 /NiO_x/Carbon ($MAPbI_3$)	12.1	W/O	Air; 40% RH	>3 months	80%	[130]
6	FTO/c-TiO_2/m-TiO_2/m-ZrO_2 /Co_3O_4/Carbon ($(5\text{-AVA})_xMA_{1-x}PbI_3$)	13.27	W/O	Air; 25°C; 70% RH	2500 h	100%	[134]
			W/O	Air; light-soaking at 100 $mW \cdot cm^{-2}$ intensity	140 h	＞90%	[134]

3.4.2 HTMs for layer-by-layer structures

Generally, the HTMs used for conventional n-i-p PSCs are likely suitable for C-PSCs with a layer-by-layer structure as well. But some HTMs are unsuited due to the following disadvantages: (1) thermal and chemical instability. When carbon paste is used to deposit CEs, the solvent in the paste and the subsequent heating can decompose the unstable HTMs, e.g. spiro-OMeTAD [45]. Moreover, some organic HTMs are susceptible to react with the migrated halide anions, resulting in declining device performance [135]. (2) Dopant hygroscopic nature. The usage of hygroscopic dopants can trigger moisture degradation of PVK [36-38]. Therefore, only chemically and thermally stable dopant-free HTMs have the potential for fabricating long-term stable C-PSCs. For layer-by-layer structures, HTMs are sandwiched between the PVK and CE in most cases, as shown in Fig. 2d. The reported HTMs include spiro-OMeTAD, poly(3-hexylthiophene) (P3HT), copper phthalocyanine (CuPc), cuprous thiocyanate (CuSCN), CuS, and NiO.

Although the PCE of devices based on spiro-OMeTAD is usually satisfactory, the devices often undergo degradation accelerated by spiro-OMeTAD's thermal instability, chemical instability, and dopant hygroscopic nature, especially under illumination and thermal stress. Gholipour et al. dropped a small amount of spiro-OMeTAD solution into carbon cloth electrodes, with the resultant device achieving a PCE of 15.29% [135]. After an MPP tracking of 115 h at 85℃ in a N_2 atmosphere, the device maintained ~50% of its initial PCE. Aitola et al. infiltrated single-walled carbon nanotube (SWCNT) networks with an appropriate amount of spiro-OMeTAD [24]. They achieved a PCE of 16.6%, and an MPP tracking of 140 h was carried out in a N_2 atmosphere. Zhang et al. spin-coated a layer of spiro-OMeTAD film prior to depositing carbon film [30]. The champion device obtained a high PCE of 19.2% and maintained over 94% of its initial PCE after an MPP tracking of 80 h at 20℃ in a N_2 atmosphere.

As a low-cost and commercialized conjugated polymer, P3HT has the following advantages: (1) ease of fabrication; (2) dopant-free oxidation process [136]; and (3)

high hydrophobicity and thermal stability [137,138]; Incorporating P3HT into carbon nanotubes (CNTs) is an effective strategy to enhance the efficiency and thermal stability of devices. Zheng et al. developed P3HT modified CNTs (CNTs@P3HT) as cathodes, with the champion device reaching a PCE of 13.43% [139]. After storage for 40 d in ambient air, the device showed a slight decline in PCE from 13.43% to 13.04%. Ahn et al. systematically investigated the effect of spiro-OMeTAD, poly[bis(4-phenyl)(2,4,6-trimethylphenyl)amine] (PTAA), and P3HT on the stability of C-PSCs [71]. These HTMs were infiltrated into the porous SWCNTs as shown in Fig. 7a, with the water vapor transmission rate (WVTR) results shown in Fig. 7b indicating that the P3HT+SWCNTs electrode was the most hydrophobic. After an MPP tracking of 2200 h under continuous illumination in air, the encapsulated device maintained 80% of its initial PCE. Chu et al. prepared a P3HT/graphene (GN) composite layer for C-PSCs and attained a certified PCE of 18.22% [140]. The device without encapsulation kept 97% of its initial PCE after storage for 1680 h in air. The encapsulated device retained 89% of its initial PCE after continuous illumination for 600 h in a N_2 atmosphere.

CuPc, a cost-effective p-type semiconductor, has been widely used as HTM in PSCs. CuPc has distinct advantages: hydrophobicity, low cost, high hole mobility (10^{-3}~10^{-2} $cm^2 \cdot V^{-1} \cdot S^{-1}$), robust chemical and thermal stability, and dopant-free utilization [141]. In 2016, Zhang et al. used dopant-free CuPc NR as HTM for the first time, with the resultant device attaining a PCE of 16.1%. [142]. After exposure to ambient atmosphere for 500 h, the PCE of the device without encapsulation declined only slightly from 16.1% to 14.7%, as shown in Fig. 7c. Liu et al. used CuPc as HTM in inorganic C-PSCs, achieving a PCE of 6.21% [143]. There was no observable decline in PCE when the devices without encapsulation were exposed to ambient atmosphere with 25℃ and 30%~40% RH for 2000 h in the dark. The same result was observed in dark ambient conditions with 100ºC and 70%~80% RH. Liu et al. fabricated planar C-PSCs using CuPc as HTM, achieving a PCE of 17.46% [144]. The relevant device showed no parametric decay after storage for 1200 h in ambient atmosphere.

CuSCN is an attractive inorganic HTM for PSCs, characterized by hydrophobicity, low cost, chemical stability, high conductivity (10^{-2}~10^{-3} $S \cdot cm^{-1}$), high hole mobility (10^{-2}~10^{-1} $cm^2 \cdot V^{-1} \cdot s^{-1}$), and a wide bandgap (3.9 eV) [145]. In 2018, Mashhoun et al. deployed CuSCN and P3HT as HTMs for C-PSCs and achieved PCEs of 12.31% and 11.58%, respectively [146]. The devices based on CuSCN and P3HT retained 80% and 60% of their initial PCEs for over 1000 h under AM1.5 light illumination in a N_2 atmosphere, respectively, as shown in Fig. 7d. Since then, the application of CuSCN in C-PSCs has been widely researched. Wu et al. improved the film morphology of CuSCN as HTM via a low-temperature dynamic spin-coating technique, with the PCE of the resultant device reaching 17.58% [122]. After exposure to continuous illumination for 1000 h in a N_2 atmosphere, the device without encapsulation maintained over 80% of its initial PCE, as shown in Fig. 7e. Arorais et al. achieved a PCE of over 18% for C-PSCs using CuSCN as HTM [147]. The device retained approximately 95% of its initial PCE after an MPP tracking of over 2000 h in a N_2 atmosphere with 60℃. The device without encapsulation kept 85% of its initial PCE after exposure to 1 $mW \cdot cm^{-2}$ UV light for over 1000 h in a N_2 atmosphere. Yang et al. infiltrated CuSCN solution into the macropores of CEs [148]. After storage for 90 d in air, the device without encapsulation showed no observable decline in PCE. After storage for 10 d in air with 70%~75% RH, the PCE only dropped by 2%.

Additionally, CuS and NiO are also commonly utilized as HTMs in C-PSCs with a layer-by-layer structure. Hu et al. incorporated CuS into CEs to enhance hole extraction and transfer, with the resultant device achieving a PCE of 11.28% [149]. After storage for 700 h in ambient air, the device without encapsulation kept 90% of its initial PCE, as shown in Fig. 7f. Sajid et al. synthesized NiO as closely-packed shells on the core carbon spheres and used them as CEs, as shown in Fig. 7g [150]. The device without encapsulation maintained a stable efficiency of 11.70% for up to 1500 h under air atmosphere with 40%~60% RH, as shown in Fig. 7h. Cai et al. prepared a thin layer of NiO on PVK film for C-PSCs and achieved a PCE of 13.6% [151]. The device without encapsulation kept 83% its initial PCE after storage for 15

d in air. The long-term stability profiles of layer-by-layer C-PSCs using different HTMs are shown in Table 6.

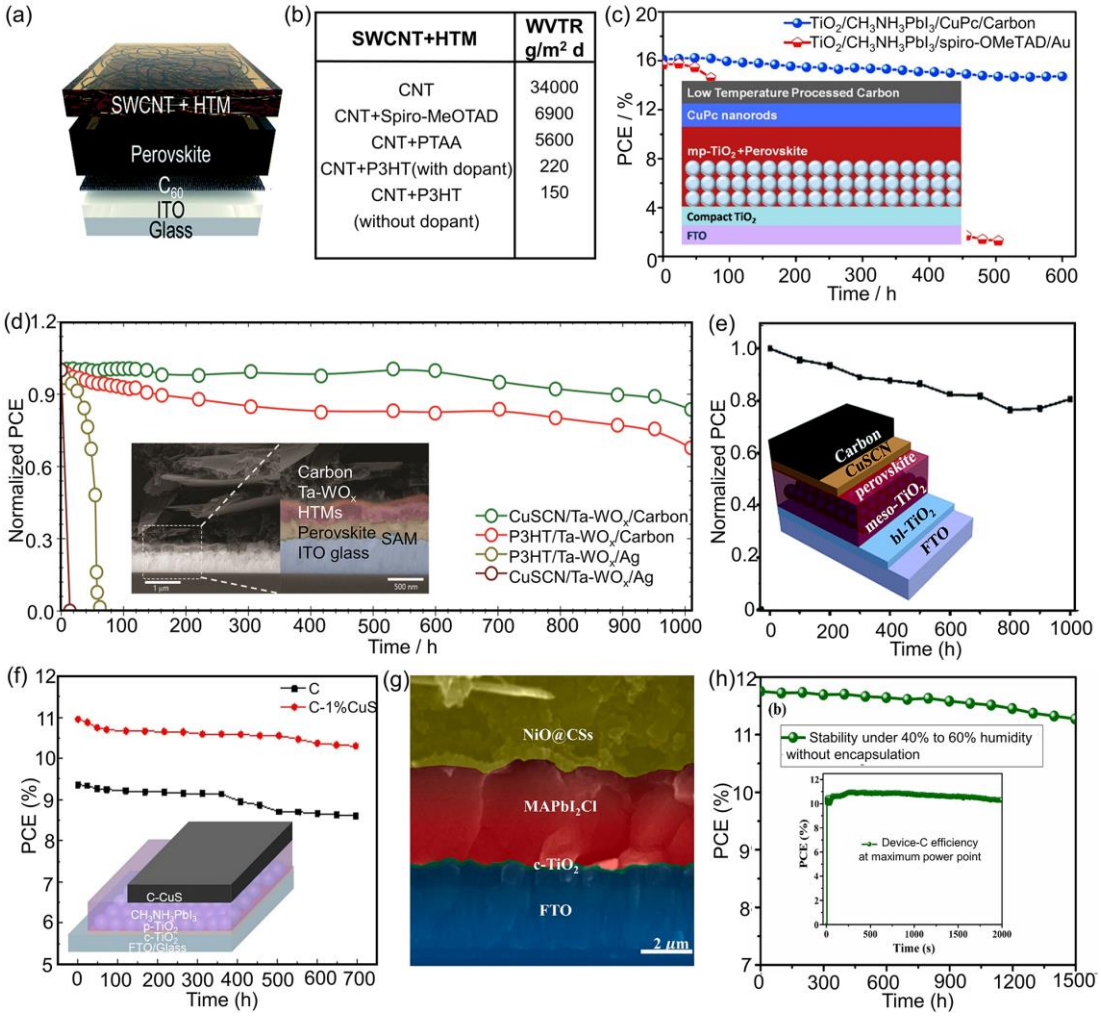

Fig.7 (a) Graphical illustration of the C-PSCs. (b) WVTR table of the SWCNT+HTMs top electrodes [71]. Reproduced from ref. 71 with permission. (c) Long-term stability of C-PSCs with CuPc as HTMs in ambient atmosphere at RT without encapsulation, the inset is the corresponding device structure [142]. Reproduced from ref. 142 with permission. (d) Photostability of C-PSCs with CuSCN and P3HT as HTMs, the inset is the cross-sectional view of the C-PSCs [146]. Reproduced from ref. 146 with permission. (e) Photostability of C-PSCs with CuSCN as HTMs, the inset is the corresponding device structure [122]. Reproduced from ref. 122 with permission. (f) Long-term stability of the PSCs based on pure C and hybrid C-CuS electrodes in ambient air with 30–50% RH without encapsulation [149]. Reproduced from ref. 149 with permission. (g) Cross-sectional SEM image of C-PSCs based on NiO@Carbon composite electrode. (h) Long-term stability of C-PSCs in ambient atmosphere at 25°C and 40%~60% RH without

encapsulation (inset is the normalized PCE at the MPP tracking for the optimized device) [150]. Reproduced from ref. 150 with permission.

Table 6 The long-term stability profiles of layer-by-layer C-PSCs using different HTMs.

No.	Device structures	Champion PCE (%)	Encapsulation	Testing environments	Time scale	Remaining value of the initial PCE	Ref.
1	FTO/c-TiO_2/m-TiO_2/ $Cs_{0.04}(MA_{0.17}FA_{0.83})_{0.96}Pb(I_{0.83}Br_{0.17})_3$ /Carbon+spiro-OMeTAD	15.29	–	N_2; 1 sun illumination (white LED); MPP tracking; 85°C	115 h	50%	[135]
2	FTO/c-TiO_2/m-TiO_2/ $Cs_{0.05}(MA_{0.17}FA_{0.83})_{0.95}Pb(I_{0.83}Br_{0.17})_3$/ Carbon+spiro-OMeTAD	16.6	–	N_2; 100 $mW\cdot cm^{-2}$ illuminations; MPP tracking; 20~60°C	140 h	–	[24]
3	FTO/c-TiO_2/m-TiO_2/ $FA_yMA_{1-y}PbI_{3-x}Br_x$/ spiro-OMeTAD/Carbon	19.2	W/O	N_2; 1 sun illumination (white LED); MPP; 20°C	80 h	94%	[30]
4	FTO/c-TiO_2/m-TiO_2/$MAPbI_3$/Carbon+P3HT	13.43	–	Air; 25°C; 20%~40% RH	40 d	97%	[139]
5	ITO/C_{60}/$MAPbI_3$/Carbon+P3HT	13.6	W	Air; 1 sun illumination including UV radiation; MPP; open-circuit condition	2200 h	80%	[71]
6	FTO/SnO_2@TiO_2/$FA_{0.3}MA_{0.7}PbI_3$ /P3HT:GN/Carbon	18.22	W/O	Air; dark condition; RT; 50％ RH	1680 h	97%	[140]
			W	N_2; 1 sun illumination (UV filter and infrared cut-off filter)	600 h	89%	[140]
7	FTO/c-TiO_2/m-TiO_2/$MAPbI_3$/CuPc/Carbon	16.1	W/O	Air; RT	600 h	91.3%	[142]
8	FTO/c-TiO_2/m-TiO_2/$CsPbBr_3$/CuPc/Carbon	6.21	W/O	Air; dark condition; 25°C; 30%~40% RH	2000 h	100%	[143]
			W/O	Air; dark condition; 100°C; 70%~80％	1000 h	100%	[143]

No.	Device structures	Champion PCE (%)	Encapsulation	Testing environments	Time scale	Remaining value of the initial PCE	Ref.
				RH			
9	FTO/Ni:TiO_2/$Cs_{0.05}(FA_{0.4}MA_{0.6})_{0.95}PbI_{2.8}Br_{0.2}$/CuPc/Carbon	17.46	W/O	Air; RT; 30%~40％ RH	1200 h	91.9%	[144]
10	FTO/C_{60} (SAM) /$MAPbI_3$/ CuSCN/Ta-WO_x/Carbon	12.31	–	N_2; AM1.5 light soaking; < 30°C	1000 h	80%	[146]
11	FTO/c-TiO_2/m-TiO_2/$Cs_{0.05}(FA_{0.4}MA_{0.6})_{0.95}PbI_{2.8}Br_{0.2}$/CuSCN/Carbon	17.58	W/O	N_2; continuous illumination (white LED) at 100 $mW\cdot cm^{-2}$ intensity	1000 h	＞80%	[122]
12	FTO/c-TiO_2/m-TiO_2/ $CsFAMAPb(I_{0.9}Br_{0.1})_3$/CuSCN/Carbon	18.1	W/O	N_2; 1 sun illumination; MPP tracking; open circuit condition; 60°C	2000 h	~95%	[147]
13	FTO/c-TiO_2/m-TiO_2/SnO_2/ $CsFAMAPb(I_{0.9}Br_{0.1})_3$/CuSCN/Carbon	18.1	W/O	N_2; continuous 1 $mW\cdot cm^{-2}$ UV illumination	1000 h	＞85%	[147]
14	FTO/SnO_2/$Cs_{0.05}FA_{0.83}MA_{0.17}PbI_{2.53}Br_{0.47}$/ Carbon+CuSCN	13.4	W/O	Air; dark condition; 23~27°C; 30%~35％ RH	>90 d	100%	[148]
			W/O	Air; dark condition; 23~27°C; 70%~75％ RH	10 d	98%	[148]
15	FTO/c-TiO_2/m-TiO_2/$MAPbI_3$/Carbon+CuS	11.28	W/O	Air; 30%~50％ RH	700 h	90%	[149]
16	FTO/c-TiO_2/$MAPbI_2Cl$/Carbon@NiO	11.7	W/O	Air; 25 °C; 40–60% RH	1500 h	99.5%	[150]
17	FTO/c-TiO_2/m-TiO_2/$MAPbI_3$/NiO/Carbon	13.6	W/O	Air	15 d	83%	[151]

3.5 Various CEs

Carbon materials have a proper work function of around –5.0 eV, which is much closer to that of Au (–5.1 eV). Moreover, CEs have the following advantages: (1) low cost and abundant sources; (2) robust hydrophobicity that can resist PVK decomposition induced by moisture; and (3) high chemical stability that can withstand PVK degradation induced by the migration of metal ions [19,23,24]. Therefore, using CEs to replace noble metal electrodes is an indispensable strategy for future commercial production of PSCs. The commonly used carbon materials include graphite [96,152], carbon black [153,154], CNTs [139,155], and biomass carbon [55,156]. Typical preparation methods of CEs include screen-printing [92,93], painting [109,110], doctor-blading [23,77], press-transfer [30,54], and lamination [157,158]. The effects of CEs on the stability of differently-structured devices are summarized below.

3.5.1 CEs for monolithic structures

For monolithic structures, since carbon paste is an essential precursor for preparing CEs, good processability of carbon materials is critical. The CEs may consist of a single, binary or multiple components of carbon materials.

First, a single component of a carbon material may be suitable to prepare CEs if certain favorable characteristics are present, namely, ease of graphitization, high electrical conductivity, and a structure beneficial for PVK precursor infiltration [156, 159]. Mali et al. prepared Aloe Vera Carbon (AV-C) electrodes, with the resultant device achieving a PCE of 12.58% [156]. The device without encapsulation retained 80% of its initial PCE after storage for 1000 h in ambient atmosphere with >65% RH, as shown in Fig. 8a. Zhong et al. developed needle coke (NC) electrodes for C-PSCs, resulting in a PCE of 11.66% [159]. The device without encapsulation maintained 90% of its initial PCE after storage for 40 d in air. Additionally, Liu et al. first deployed a thin film (~1.8 μm) of SWCNTs as back contact for a monolithic structure, achieving a PCE of 12.7% and observing good stability for 300 h in dark ambient conditions

[160]. Luo et al. fabricated a novel device based on a substrate/NiO(PVK)/Al_2O_3(PVK)/SnO_2@CNTs(PVK) structure, attaining a PCE of 14.3% [161]. The device retained over 88% of its initial PCE for 550 h under full light soaking in a N_2 atmosphere.

Second, a binary mixture of graphite and carbon black is often used to prepare CEs. The ratio between the graphite and carbon black plays a key role in determining the mesoporous structure and electrical conductivity, thus influencing the infiltration of the PVK precursor and charge transfer [92,162]. Extensive researches have been conducted on the stability of C-PSCs prepared with a binary mixture of graphite and carbon black [19,31,88,91,99,100,104,107,108,129]. To date, for laboratory-scale cells, a maximum PCE of ~17% has been achieved [108]. The long-term environmental stability of the cells without encapsulation has topped over 4500 h in ambient atmosphere [129]; the photostability has reached ~1000 h under continuous 100 $mW \cdot cm^{-2}$ illumination [100]; and the thermal stability of the encapsulated device has risen to ~1000 h at 85ºC in the dark [108]. For large-scale PSMs shown in Fig. 8b, the PCE has reached 10%. The encapsulated module has been recorded to achieve long-term stability for over one year in the dark [91], photostability for ~10000 h under 1 sun illumination at 55ºC [31], and operational stability for ~1000 h under continuous AM1.5 illumination at MPP in ambient air [91]. Overall, C-PSCs with binary mixture electrodes have exhibited outstanding long-term stability.

Third, multiple component electrodes usually consist of graphite, carbon black, and functional additives, which facilitate energy level alignment and improve back contact conductivity. Recently, Zhou et al. doped the mixture of graphite and carbon black with WO_3 nanoparticles, resulting in a PCE increase from 7% to 10.8% and showing excellent long-term stability for over 150 d in air, as shown in Fig. 8c [163]. Bhandari et al. also demonstrated the positive effect of WO_3 on stability [164]. The addition of a certain amount of WO_3 nanoparticles was shown to enhance the photostability of the device without encapsulation from 350 h to over 500 h. Li et al. sprayed a thin layer of MWCNTs on the top of the graphite and carbon black

composites as shown in Fig. 8d, improving both the conductivity and charge transfer characteristic of the electrode [165]. The device without encapsulation retained >80% of its initial PCE after storage for 500 h in ambient atmosphere. The long-term stability profiles of C-PSCs using CEs with different components are shown in Table 7.

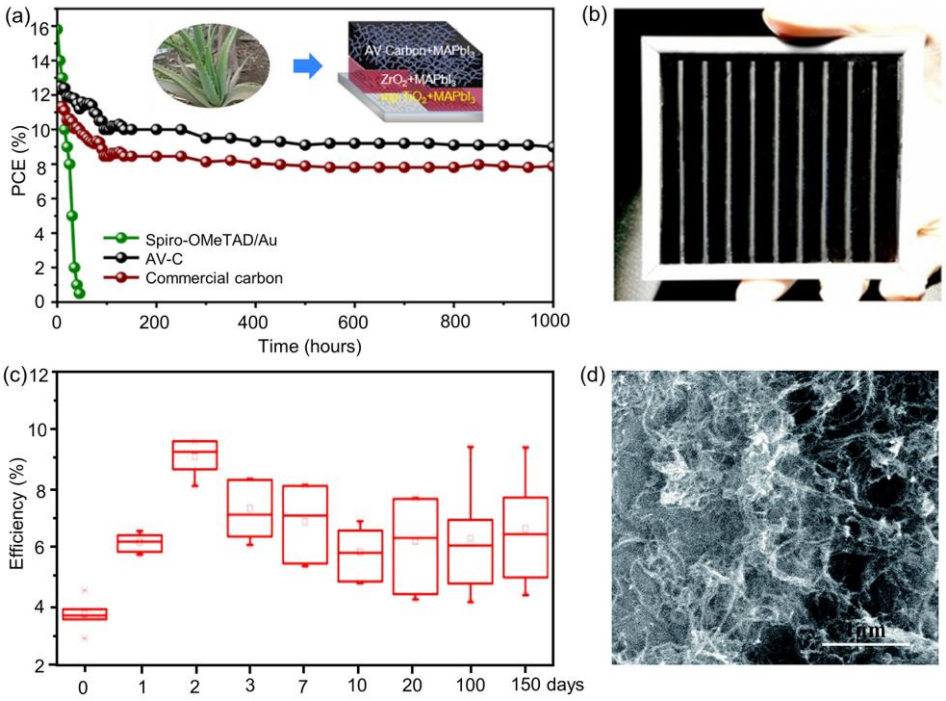

Fig.8 (a) Long-term stability of AV-C, commercial carbon paste, and spiro-OMeTAD/Au based PSCs under ambient condition with 65 % RH, the inset is schematic illustration of C-PSCs based on AV-C electrodes [156]. Reproduced from ref. 156 with permission. (b) Image of a 10×10 cm^2 carbon-based PSM, where the CE is made of graphite+carbon black composite [91]. Reproduced from ref. 91 with permission. (c) Long-term stability of a batch of PSCs (10 cells) using CEs with WO_3 additive in ambient atmosphere [163]. Reproduced from ref. 163 with permission. (d) The top view SEM image of MWCNT layer [165]. Reproduced from ref. 165 with permission.

Table 7 The long-term stability profiles of monolithic C-PSCs using CEs with different components.

No.	Device structures	Champion PCE (%)	Composition of CEs	Encapsulation	Testing environments	Time scale	Remaining value of the initial PCE	Ref.
1	FTO/c-TiO_2/m-TiO_2/ m-ZrO_2/Carbon ($MAPbI_3$)	12.58	Aloe Vera Carbon	W/O	Air; RT; 30%~65% RH	1000 h	＞80%	[156]
2	FTO/c-TiO_2/m-TiO_2/ m-ZrO_2/Carbon ($(5\text{-}AVA)_x(MA)_{1-x}PbI_3$)	11.66	Needle coke	W/O	Air; RT; 40%~60% RH	40 d	90%	[159]
3	FTO/c-TiO_2/m-TiO_2/ m-Al_2O_3/NiO/Carbon ($MAPbI_3$)	12.7	CNTs	W/O	Air; dark condition; RT; 40%~60% RH	300 h	100%	[160]
4	FTO/NiO/Al_2O_3/SnO_2@Carbon ($MAPbI_3$)	14.3	CNTs	–	N_2; AM 1.5G illumination	550 h	88%	[161]
5	FTO/c-TiO_2/m-TiO_2/ m-ZrO_2/Carbon ($(5\text{-}AVA)_x(MA)_{1-x}PbI_3$)	10.4	Graphite+ carbon black	W/O	Air; continuous AM1.5 illumination; MPP; 25°C; 54% RH	1000 h	100%	[91]
				W/O	Dark condition	>1 year	100%	[91]
6	FTO/c-TiO_2/m-TiO_2/ m-ZrO_2/Carbon ($(5\text{-}AVA)_2PbI_4/MAPbI_3$)	11.16	Graphite+ carbon black	W	1 sun illumination (UV filter); 55°C	10000 h	100%	[31]

No.	Device structures	Champion PCE (%)	Composition of CEs	Encapsulation	Testing environments	Time scale	Remaining value of the initial PCE	Ref.
7	FTO/c-TiO_2/m-TiO_2/ m-ZrO_2/Carbon ($((5\text{-AVA})_x(MA)_{1-x}PbI_3$)	8.47	Graphite+ carbon black	W/O	Continuous 100 mW·cm^{-2} illumination (UV filter); open circuit condition; 35ºC	1046 h	95.5%	[100]
8	FTO/c-TiO_2/m-TiO_2/ m-Al_2O_3/NiO/Carbon ($Cs_{0.05}(FA_{0.4}\ MA_{0.6})_{0.95}PbI_{2.8}Br_{0.2}$)	17.02	Graphite+ carbon black	W	Dark condition; 85°C; 40%~60％ RH	1000 h	91%	[108]
9	FTO/c-TiO_2/m-TiO_2/ m-ZrO_2/Cu:NiO/Carbon ($MAPbI_3$)	13.74	Graphite+ carbon black	W/O	Air; 25°C; 65% RH	>4500 h	90%	[129]
10	FTO/c-TiO_2/m-TiO_2/ m-Al_2O_3/WO_3:Carbon ($MAPbI_3$)	10.77	WO_3+ graphite+ carbon black	W/O	Air	3600 h	–	[163]
11	FTO/c-TiO_2/m-TiO_2/ m-Al_2O_3/WO_3:Carbon ($MAPbI_3$)	10.5	WO_3+ graphite+ carbon black	W/O	Air; light illumination	500 h	85%	[164]
12	FTO/c-TiO_2/m-TiO_2/ m-Al_2O_3/Carbon ($((5\text{-AVA})_{0.05}\ (MA)_{0.95}PbI_3$)	11.31	CNTs+ graphite+ carbon black	W/O	Air; RT	500 h	85%	[165]

3.5.2 CEs for layer-by-layer structures

For layer-by-layer structures, the PVK or HTM film is usually prepared prior to the deposition of the CEs. Subsequently, the carbon paste or a separate carbon layer is doctor-bladed or press-transferred atop them. The choice for the carbon materials is extensive, including biomass carbon, graphite, carbon black, and CNTs, among others. We summarize the relevant work in the following order: biomass carbon materials, graphite and carbon black composites, CNTs, and separate carbon films.

In 2014, Wei et al. developed a low-cost bio-carbon electrode made from candle soot, with the resultant device achieving a PCE of 11.02% [166]. After storage for 30 d in ambient air, the device without encapsulation retained 85% of its initial PCE. Our group fabricated ultra-low-cost, eco-friendly coal-, corn stalk-, peanut shell-, phragmites australi-, and bamboo chopstick-based electrodes [55,167]. High efficiency and good stability were achieved in the devices based on the bamboo chopsticks. After storage for 2000 h in ambient air, the device without encapsulation maintained 87% of its initial PCE, as shown in Fig. 9a.

Although bio-carbon materials are low-cost and eco-friendly, their conductivity is usually poorer due to the low graphitization of amorphous carbon. Carbon paste made of graphite and carbon black is thus widely used to prepare CEs due to its low cost, high conductivity, and ease of doctor-blading or screen-printing [168,169]. In 2014, our group reported low-temperature CEs made from conductive carbon paste for PSCs [23]. The contact angle tests indicated strong hydrophobicity of the CEs. The resultant device showed excellent environmental stability for 2000 h. Chu et al. designed a low-temperature perovskite-friendly composite paste of graphite and carbon black for paintable PSCs, achieving a PCE of 13.5% [89]. The device without encapsulation retained >90% of its initial PCE after storage for 960 h in ambient atmosphere with RT and 50% RH. However, graphite and carbon black composite may suffer from poor energy level alignment and charge transport. To solve this problem, Ding et al. doped the carbon paste with Pt:Ni alloy nanowires for inorganic C-PSCs, with the resultant device reaching a PCE of 7.86% [170]. After storage for

20 d in air (80% RH), the device without encapsulation showed no significant degradation. Zhang et al. utilized a novel vibration technology to make the carbon layer denser, with the device achieving a PCE of 11.49% and showing good stability [171]. Wang et al. doped CNTs in both the PVK precursor and carbon paste to create rapid pathways for charge transfer, with the resultant device achieving a PCE of 15.73% [172]. After storage for 90 d in the dark, the devices without encapsulation showed no degradation whether in high humidity (65±5% RH) or in high temperature (75±5ºC) conditions. Unlike the above-mentioned pre-treatments of CEs, Kim et al. reported a post-treatment of CEs using C_4F_8 vacuum fluorine plasma, fabricating a device with a PCE of 14.86% [173]. Owing to the synergistic effect between the hydrophobic fluorine atoms and the CEs, the device retained 95% of its initial PCE after storage for 1000 h in air, as shown in Fig. 9b. Liu et al. developed a simple post-treatment for CEs using acetate salt [174]. The device without encapsulation retained its initial PCE for at least 4 months in air. Although excess moisture induces decomposition of the PVK crystals, the rationally-controlled atmospheric humidity may extend the lifetime of C-PSCs. Yan et al. reported a moisture-assisted post-annealing (MAPA) treatment, with the device that was treated for 2 h in a 30% RH atmosphere obtaining a PCE of 14.77% [175]. The device without encapsulation showed no significant degradation after storage for 150 d in dark ambient conditions.

Carbon cloth and carbon fiber are widely used as catalysts or counter electrodes in dye-sensitized solar cells, lithium batteries, and supercapacitors. Gholipour et al. deployed a low-cost carbon cloth electrode as a hole collector composite and degradation inhibitor for PSCs [135]. The resultant device achieved a PCE of 15.29%. While the use of carbon materials as back contact could avoid migration of noble metal ions to PVK, the chemical reaction between spiro-$OMeTAD^+$ and migrating I^- possibly triggered the slow degradation of the device. After an MPP tracking of 115 h under continuous 100 $mW \cdot cm^{-2}$ illumination at 85℃ in a N_2 atmosphere, the device lost about 50% of its initial PCE.

Under normal temperature and pressure, the intrinsic work function of CNTs is

about 4.7~5.1 eV, exhibiting p-type semiconducting characteristics. In the past few years, this has spotlighted CNTs potential to perform excellently as HTM and back electrodes in C-PSCs. Wei et al. adopted MWCNTs as back electrodes for C-PSCs, with the device reaching a PCE of 12.67% and keeping ~90% of its initial PCE after storage for 10 d in the dark [152]. Luo et al. incorporated iodine doped cross-stacked superaligned carbon nanotube (CSCNT) sheets into PSCs, achieving a PCE of 10.54% [176]. The encapsulated devices kept >93% of its initial PCE after storage for 1500 h in dark ambient conditions, and retained >87% of its initial PCE for 400 h under continuous illumination in air. Zheng et al. synthesized boron doped MWCNTs as the back contact, achieving a PCE of 15.23% [155]. The device without encapsulation retained 98% of its initial PCE after storage for 80 d in dry air, 85% of its initial PCE after storage for 14 d in an oven at 80℃, and 93% of its initial PCE after storage for 14 d in a high-humidity atmosphere with 60% RH. Aitola et al. designed a composite layer of spiro-OMeTAD+SWCNTs as the back contact, with the resultant device attaining a PCE of 16.6% [24]. After an MPP tracking under continuous illumination in a N_2 atmosphere, the lifespan of the device was estimated to be approximately 580 h. Importantly, their results powerfully confirmed that using CNTs as back contact could impede PVK degradation induced by moisture and ion migration of noble metals. Although CNTs are widely considered a promising material, its shallow work function and non-reflective nature have thus far limited significant performance improvements of CNT-based PSCs. Lee et al. developed vapor-assisted ex-situ doping of CNT for more efficient and stable PSCs, as shown in Fig. 9c [177]. The device based on trifluoromethanesulfonic acid (TFMS) doped CNTs achieved a PCE of 17.6%, with the encapsulated devices maintaining 86.9% of their initial PCE after continuous operation for 244 h in a N_2 atmosphere with 60±5℃ and 50%±10% RH, as shown in Fig. 9d. The TFMS doping behavior further enhanced the hydrophobicity of CNTs films, as shown in Fig. 9e. Luo et al. used CSCNTs as the back electrodes for flexible PSCs [178]. The devices retained 92% of their initial PCE after exposure to continuous illumination for 1014 h, and kept 89% of their initial PCE after continuous heating at 60°C for 1570 h in dark ambient conditions. Although p-i-n planar PSCs are

becoming more and more attractive due to their easy preparation and small hysteresis effect, their long-term stability is hampered due to the ionic migration between the noble metal electrode and the PVK layer. To deal with this issue, Zhou et al. used polyethylenimine (PEI) modified CSCNTs films as back contact for the inverted devices [28]. After storage for 500 h in air, the device without encapsulation maintained over 94% of its initial PCE. When elevating the atmospheric temperature and humidity to 60℃ and 60% RH, respectively, the encapsulated device maintained 85% of its initial PCE after storage for 500 h.

In addition, the development of separate carbon films provides a distinct strategy for achieving long-term stable PSCs, avoiding the issue of solvents in the carbon paste damaging the PVK or HTM layers. In 2015, Wei et al. developed a free-standing carbon film as back contact, with the resultant device achieving a PCE of 13.53% [54]. After storage for 20 d in ambient atmosphere, the PCE decreased from 13.53% to 12.87%. Zhang et al. designed a self-adhesive carbon film as back electrodes (Fig. 9f), with the PCE of the resultant device attaining 19.2% [30]. The device without encapsulation retained over 95% of its initial PCE after storage for 1000 h in ambient atmosphere, and kept over 94% of its initial performance after an MPP tracing of 80 h in a N_2 atmosphere, as shown in Fig. 9g-h. Recently, Su et al. developed a self-adhesive macroporous carbon film to match with the practical square-centimeter scale devices [179]. They achieved a PCE of 17.02% on the active area of 1 cm^2. After storage for 1500 h at 20°C and 30% RH in the dark, the device without encapsulation retained 90.5% of its initial PCE. The long-term stability profiles of C-PSCs using various CEs are shown in Table 8.

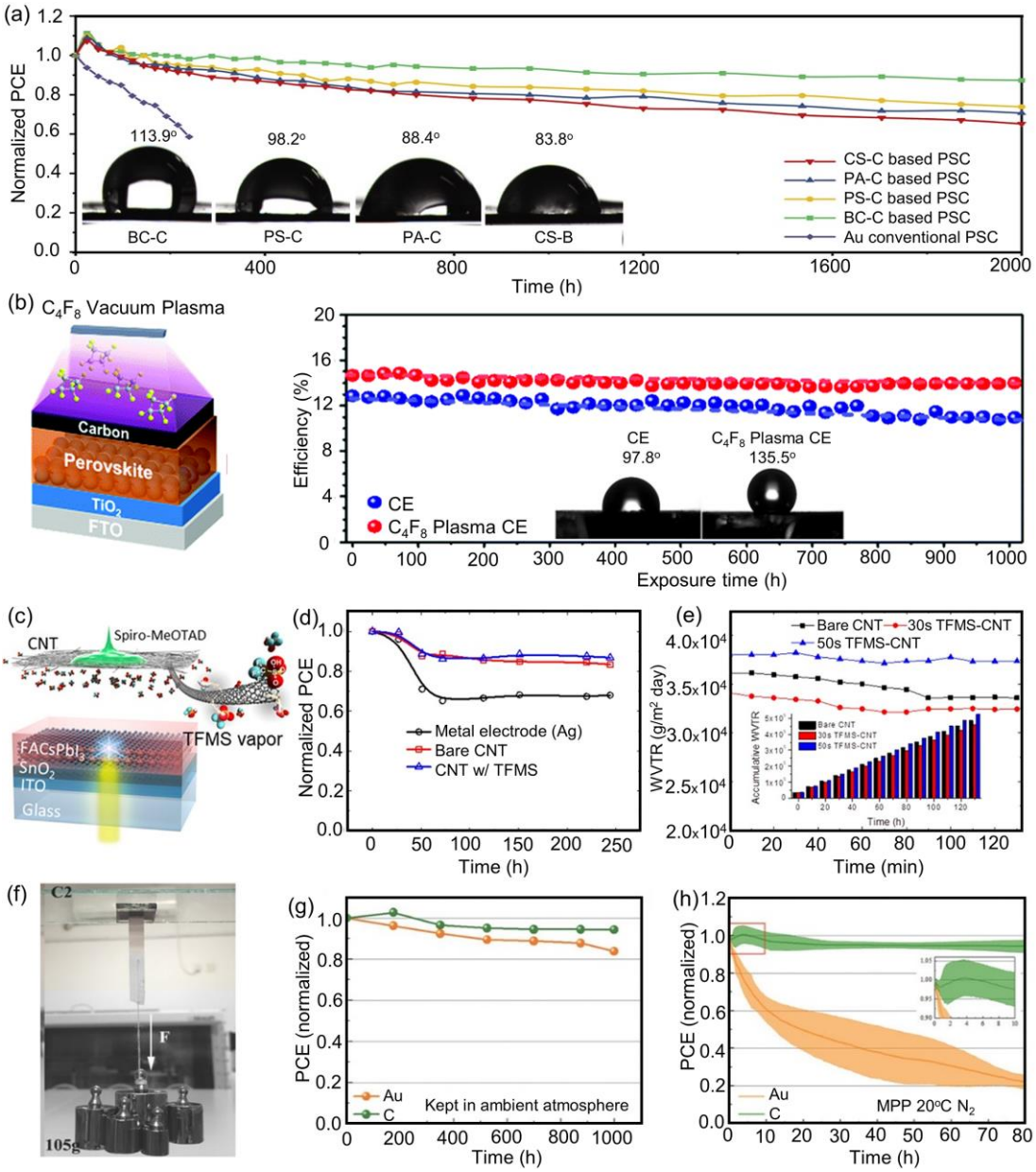

Fig.9 (a) Stability tests of PSCs with bio-carbon electrodes and conventional PSCs in ambient atmosphere with 30% RH at RT; the inset is contact-angle tests that were carried out on PSCs based on different bio-carbon CEs [167]. Reproduced from ref. 167 with permission. (b) Schematic illustration of the C-PSCs with CEs treated by C_4F_8 vacuum plasma, and long-term stability of devices based on CEs with and without C_4F_8 vacuum plasma treatment under controlled ambient conditions (25°C; 40 %± 5% RH), the inset is the corresponding results of contact angle test [173]. Reproduced from ref. 173 with permission. (c) Schematic illustration of planar heterojunction perovskite solar cells using TFMS doped CNT as back electrode. (d) PCE evolution of the encapsulated devices under continuous 1 sun illumination at open-circuit condition (60±5°C, 50%±10% RH). (e) Water vapor transmittance rates (WVTRs) of bare CNT

(black) film, 30 s vapor-doped CNT film (red), and 50 s vapor-doped CNT film (blue) [177]. Reproduced from ref. 177 with permission. (f) Adhesive force test of the self-adhesive carbon film by gravity experiment. (g) Stability test of the PSCs in ambient atmosphere without any encapsulation. (h) Aging test of the PSCs under constant illumination at MPP in a N_2 atmosphere with 20^{o}C [30]. Reproduced from ref. 30 with permission.

Table 8 The long-term stability profiles of layer-by-layer C-PSCs using various CEs.

No.	Device structures	Champion PCE (%)	Composition of CEs	Encapsulation	Testing environments	Time scale	Remaining value of the initial PCE	Ref.
1	FTO/c-TiO_2/m-TiO_2/$MAPbI_3$/Carbon	11.02	Candle soot	W/O	Air; RT; 20% RH	30 d	83%	[166]
2	FTO/c-TiO_2/m-TiO_2/$Cs_{0.05}(MA_{0.17}FA_{0.83})_{0.95}Pb(I_{0.83}Br_{0.17})_3$ /Carbon	10.87	Coal powder	W/O	Air; dark condition; RT; 30% RH	120 h	84.4%	[55]
3	FTO/c-TiO_2/m-TiO_2/$Cs_{0.05}(MA_{0.17}FA_{0.83})_{0.95}Pb(I_{0.83}Br_{0.17})_3$/Carbon	12.82	Bamboo chopstick	W/O	Air; dark condition; 25°C; 30% RH	2000 h	87%	[167]
4	FTO/c-TiO_2/m-TiO_2/MAPbI3/Carbon	9.08	Graphite+ carbon black	W/O	Air; dark condition	2000 h	100%	[23]
5	FTO/c-TiO_2/m-TiO_2/$MAPbI_3$/Carbon	13.5	Graphite+ carbon black	W/O	Air; RT; 50% RH	960 h	>90%	[89]
6	FTO/c-TiO_2/m-TiO_2/$CsPbBr_3$/Carbon	7.86	Pt:Ni+ graphite+ carbon black	W/O	Air; 25°C; 80％ RH	20 d	100%	[170]
7	FTO/c-TiO_2/m-TiO_2/$MAPbI_3$/Carbon	11.49	Graphite+ carbon black	W/O	Air; RT; ⩽40% RH	15 d	100%	[171]
8	FTO/c-TiO_2/m-TiO_2/$MAPbI_3$:CNTs/ Carbon	15.73	CNTs+ graphite+ carbon black	W/O	Air; dark condition; 25±5°C; 65%±5% RH	90 d	100%	[172]
				W/O	Air; dark condition; 75±5°C; 25%±5% RH	90 d	100%	[172]

No.	Device structures	Champion PCE (%)	Composition of CEs	Encapsulation	Testing environments	Time scale	Remaining value of the initial PCE	Ref.
9	FTO/c-TiO_2/m-TiO_2/ $Cs_{0.05}MA_{0.16}FA_{0.79}Pb(I_{0.84}Br_{0.16})_3$/Carbon	14.86	Graphite+ carbon black	–	Air; 25°C; 40% ± 5% RH	1000 h	95%	[173]
10	FTO/c-TiO_2/m-TiO_2/ $MAPbI_3$:$MA_{1-x}Cs_xPbI_3$/Carbon	15.27	Graphite+ carbon black	W/O	Air; ~50% RH	>4 months	100%	[174]
11	FTO/SnO_2/$FA_{1-z}MA_zPb(I_{1-x-y}Br_xCl_y)_3$/Carbon	14.77	Graphite+ carbon black	W/O	Air; RT; 45%±10% RH	150 d	100%	[175]
12	FTO/c-TiO_2/m-TiO_2/ $Cs_{0.04}(MA_{0.17}FA_{0.83})_{0.96}Pb(I_{0.83}Br_{0.17})_3$ /Carbon+spiro-OMeTAD	15.29	Carbon cloth+ graphite+ carbon black	–	N_2; 1 sun illumination (white LED); MPP tracking; 85°C	115 h	50%	[135]
13	FTO/c-TiO_2/m-TiO_2/$MAPbI_3$/Carbon	12.67	MWCNTs	–	Dark condition; RT; 20% RH	10 d	90%	[152]
14	FTO/c-TiO_2/m-TiO_2/m-Al_2O_3/$MAPbI_3$/Carbon	10.54	Iodine doped CSCNT	W	Air; dark condition; 45°C; 75% RH	1500 h	>93%	[176]
				W	Air; light soaking at 100 mW·cm^{-2} intensity; 20±6°C; 30%±7% RH	400 h	>87%	[176]
15	FTO/c-TiO_2/m-TiO_2/m-Al_2O_3 $MAPbI_3$/Carbon	15.23	B:MWCNTs	W/O	Air; dark condition	80 d	98%	[155]
				W/O	Air; dark condition; 80°C	14 d	85%	[155]
				W/O	Air; 25°C; 60% RH	14 d	93%	[155]

No.	Device structures	Champion PCE (%)	Composition of CEs	Encapsulation	Testing environments	Time scale	Remaining value of the initial PCE	Ref.
16	FTO/c-TiO_2/m-TiO_2/ $Cs_{0.05}(MA_{0.17}FA_{0.83})_{0.95}Pb(I_{0.83}Br_{0.17})_3$/ Carbon+spiro-OMeTAD	16.6	SWCNTs	–	N_2; continuous 100 mW·cm^{-2} illumination; MPP tracking; 20~60°C	580 h	80%	[24]
17	ITO/SnO_2/ $FACsPbI_3$/ spiro-OMeTAD/Carbon	17.56	TFMS:CNTs	W	N_2; continuous 100 mW·cm^{-2} illumination; open-circuit condition; 60 ± 5°C; 50% ± 10% RH	244 h	86.9%	[177]
18	PEN/GN/c-TiO_2:$PC_{61}BM$/$MAPbI_3$/ Carbon+spiro-OMeTAD	11.9	CSCNTs	–	Air; 100 mW·cm^{-2} illumination (without UV filter); 19±3°C; 38% ± 6 % RH	1014 h	92%	[178]
				–	Air; dark condition; 60°C; 38%±6% RH	1570 h	89%	[178]
				W/O	Air; 20~30°C; 10%~50% RH	500 h	＞94%	[28]
19	FTO/NiO_x/$MAPbI_3$/$PC_{61}BM$/Carbon	10.84	PEI:CSCNTs	W/O	Air; 60°C; 10%~50% RH	500 h	90%	[28]
				W	Air; 60°C; 60% RH	500 h	85%	[28]
20	FTO/c-TiO_2/m-TiO_2/$MAPbI_3$/ Carbon	13.53	Free-standing carbon film	W/O	Air; RT	20 d	95.1%	[54]
21	FTO/c-TiO_2/m-TiO_2/ $FA_yMA_{1-y}PbI_{3-x}Br_x$/spiro-OMeTAD/Carbon	19.2	Self-adhesive carbon film	W/O	Air; dark condition; 25°C; 30% RH	1000 h	95%	[30]

No.	Device structures	Champion PCE (%)	Composition of CEs	Encapsulation	Testing environments	Time scale	Remaining value of the initial PCE	Ref.
				W/O	N_2; 1 sun illumination (white LED); MPP tracking; 20^{o}C	80 h	94%	[30]
22	FTO/SnO_2/ $Cs_{0.05}(FA_{0.85}MA_{0.15})_{0.95}Pb(I_{0.85}Br_{0.15})_3$/ spiro-OMeTAD/Carbon	17.02	Self-adhesive carbon film	W/O	Air; dark condition; 20°C; 30% RH	1500 h	90.5%	[179]

4. Strengthening encapsulation

To minimize the environmental risks that can trigger device degradation, one of the most effective strategies is to strengthen encapsulation [48,49]. To date, the relevant techniques with regards to C-PSCs fall into two categories: laboratory-scale cells and large-scale carbon-based PSMs. The effects of encapsulation techniques on device stability are summarized below.

4.1 Laboratory-scale cells

Laboratory-scale cells can flexibly be encapsulated within a limited active area. A wide array of encapsulation techniques exists, including thin glass+UV-curable resin, polydimethylsiloxane (PDMS) protective layer, epoxy+Ag-paint protective layer, and epoxy resin protective layer.

In 2015, Cao et al. reported that the C-PSCs sealed with thin glass+UV-curable resin retained more than 75% of their initial PCE for 1000 h under continuous light soaking in ambient atmosphere at RT (~25°C) and 40% RH, showing excellent stability [124]. Baranwal et al. found that a proper sealing position was required for the devices to avoid rapid degradation under thermal stress, as shown in Fig. 10a [180]. The sealed devices maintained about 90% of their initial PCE for 4500 h in ambient atmosphere [44]. Similarly, Ahn et al. used thin glass+UV-curable resin to encapsulate the C-PSCs, with the resultant device keeping up to 80% of its initial PCE after storage for 2200 h under 1 sun illumination including UV radiation in ambient air, as shown in Fig. 10b [71]. Additionally, Liu et al. simply sealed the C-PSCs using PDMS [181]. After storage in air for 3000 h at 20℃ and 20% RH, the PCE of the device showed a slight increase. Wei et al. elaborately designed an epoxy+Ag-paint protective layer on top of the CE [182]. The devices were tested in different environmental conditions to assess water resistance. They found that the devices maintained stable operation in a watery environment for 80 min. Hashmi et al. encapsulated C-PSCs using low-cost epoxy resin [183]. After continuous exposure to

150 mW·cm^{-2} UV light for 1002 h, the encapsulated device showed no performance decline, as shown in Fig. 10c.

4.2 Large-scale PSMs

For large-scale PSMs, the encapsulation techniques are extremely challenging because of the unsuitability of the edge sealing method. Likewise, common encapsulation techniques for silicon or thin-film solar cells are not applicable due to the high-temperature decomposition of PVK materials. The currently reported encapsulation techniques include glass+Pattex silicon, glass+Surlyn polymer, and glass+hot melt polyurethane (PU) film.

In 2017, Hu et al. sealed large-scale PSMs (substrate area: 100 cm^2) using glass+Pattex silicon and conducted an outdoor stability test [91]. The encapsulated PSM showed no decay in performance after exposure outdoors at ~30°C and ~80% RH. Grancini et al. encapsulated PSMs (substrate area:100 cm^2) using glass+DuPont Surlyn polymer [31]. The module was covered with a thin glass, and the edges were plugged using DuPont Surlyn polymer. Then, an extra layer of epoxy glue was added around the edges of the module. The encapsulated PSM showed no decline in performance for over 10,000 h under continuous illumination in air at 55^{o}C. Although the stability of the PSMs was decent, the effects of the encapsulation on device performance were not well studied and discussed in the above-mentioned reports. Recently, Fu et al. systematically investigated the encapsulation process, including laminating temperature, selection of hot melt films, film thickness, and melting temperatures [184]. They developed an encapsulation technique using glass+hot melt PU film, which was suitable for PSMs. The PSM maintained 97.52% of its initial PCE after exposure outdoors for over 2000 h, as shown in Fig. 10d. This demonstrates the huge potential of the studied encapsulation technique in the commercial development of PSCs. The long-term stability profiles of C-PSCs using different encapsulation techniques are shown in Table 9.

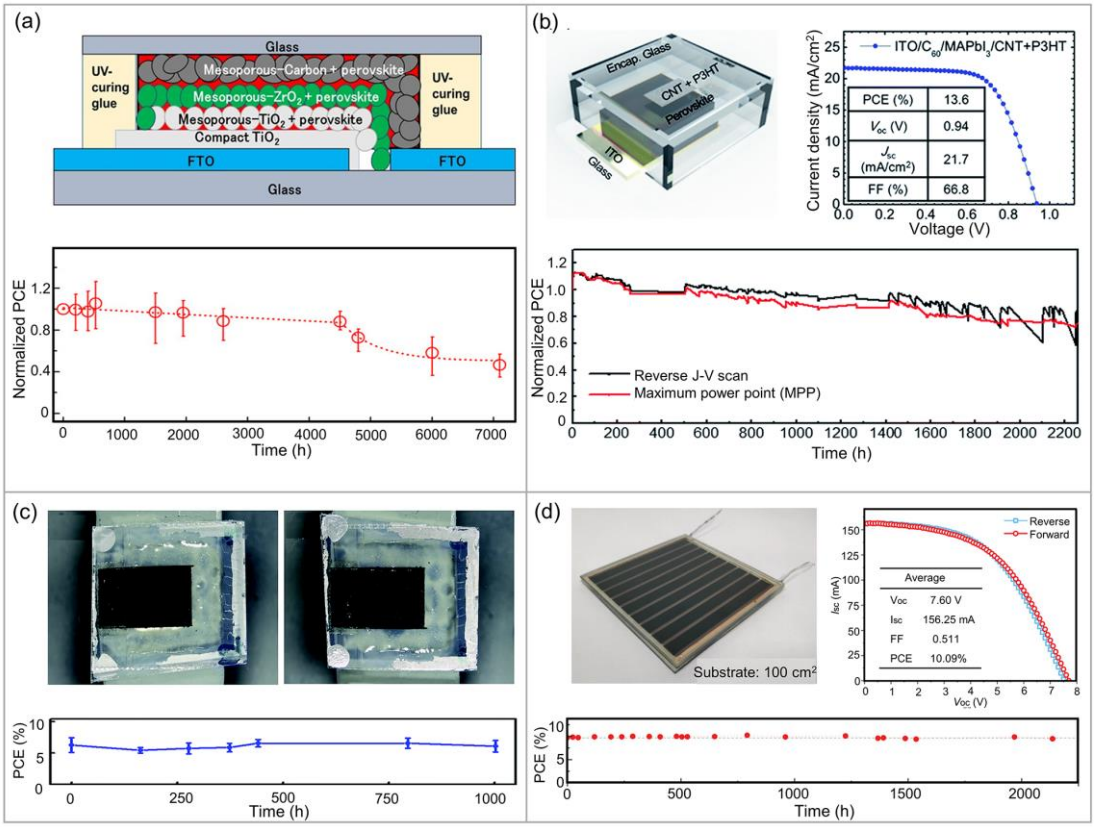

Fig.10 (a) Diagram of the side-sealed C-PSCs with a monolithic structure [180], and the PCE evolution of the device under thermal stress at 100 °C for over 7000 h [44], respectively. Reproduced from ref. 180 and ref. 44 with permission. (b) Illustration, J–V curve, and PCE evolution of the encapsulated device using a thin glass+UV-curable resin technique [71]. Reproduced from ref. 71 with permission. (c) Photographs of the front side (left) and back side (right) of the sealed device using an epoxy resin layer, and PCE evolution of the device under continuous 1.5 sun equivalent UV light illumination in air environment [183]. Reproduced from ref. 183 with permission. (d) The digital image of a carbon-based PSM (100 cm^2; active area of 60.09 cm^2) encapsulated with a PU film as the sealant and a glass sheet as the back cover, J–V curves and PCE evolution of the PSM under outdoor conditions (location: 39°19′48″N 114°37′26″E) [184]. Reproduced from ref. 184 with permission.

Table 9 The long-term stability profiles of C-PSCs using different encapsulation techniques

Item	Device structures	Champion PCE (%)	Encapsulation techniques	Testing environments	Time scale	Remaining value of the initial PCE	Ref.
Laboratory-scale cells	FTO/c-TiO_2/m-TiO_2/Al_2O_3/NiO/Carbon ($MAPbI_3$)	15.03	Thin galss+ UV-curable resin	Air; light soaking (white LED) at 100 $mW \cdot cm^{-2}$ intensity; ~25°C; ~40% RH	1000 h	＞75%	[124]
	FTO/c-TiO_2/m-TiO_2/m-ZrO_2/Carbon ($MAPbI_3$)	4.93	Thin galss+ UV-curable resin	Air; dark condition; 100°C	7000 h	40%	[44]
	ITO/C_{60}/$MAPbI_3$/CNTs+P3HT	13.6	Thin galss+ UV-curable resin	Air; 1 sun illumination including UV radiation; MPP	2200 h	80%	[71]
	FTO/c-TiO_2/m-TiO_2/$MAPbI_3$/Carbon	10.8	PDMS protective layer	Air; ~20°C; 20% RH	3000 h	109%	[181]
	FTO/ c-TiO_2/m-TiO_2/$MAPbI_3$ /Carbon	10.99	Epoxy+Ag-paint protective layer	Air; 60%~80% RH Water soaking 50°C; 70%~90% RH	20 d 80 min 250 h	100% 100% 100%	[182] [182] [182]
	FTO/c-TiO_2/m-TiO_2/m-ZrO_2/Carbon $(5\text{-AVA})_xMA_{1-x}PbI_3$)	6.2	Epoxy resin protective layer	Air; continuous 1.5 sun equivalent UV light illumination; open circuit condition; 40°C; 45% RH	1002 h	100%	[183]
Large-scale PSMs	FTO/c-TiO_2/m-TiO_2/m-ZrO_2/Carbon $(5\text{-AVA})_xMA_{1-x}PbI_3$)	10.4	Glass+ Pattex silicon	Outdoor environment; ~30°C; ~80% RH	1 month	100%	[91]
	FTO/c-TiO_2/m-TiO_2/m-ZrO_2/Carbon ($(5\text{-AVA})_2PbI_4$/$MAPbI_3$)	11.16	Glass+ Surlyn polymer	1 sun illumination with UV filter; 55°C	> 10000 h	100%	[31]
	FTO/c-TiO_2/m-TiO_2/m-ZrO_2/Carbon $(5\text{-AVA})_xMA_{1-x}PbI_3$)	10.09	Galss+hot melt PU film;	Outdoor environment; natural sunlight; working condition; −10~35°C	2136 h	97.52%	[184]

5. Conclusion and Outlook

C-PSCs have achieved a decent PCE of ~20% and one-year stability, making them one of the most promising candidates for the commercialization of PVK photovoltaics. Yet, the stability of C-PSCs still lags behind the expected 25-year lifespan of the commercialized silicon and thin-film photovoltaics. It is thus imperative to carry out further studies on the stability of C-PSCs. In this review, we have summarized the environmental risks affecting the long-term stability of C-PSCs and the key strategies for achieving the same. Main factors affecting stability include moisture, oxygen, light, thermal stress, and their synergistic effects under atmospheric conditions. To minimize the environmental risks triggering device degradation, strategies for greater stability can be divided into two aspects: improving the intrinsic stability and strengthening encapsulation. With regards to the former, multiple strategies have been developed to improve the intrinsic stability of C-PSCs, including proper TCO substrates, selection of ETMs, composition engineering of PVK photoabsorbers, suitable HTMs, and different materials for CEs. With regards to the latter, various encapsulation techniques for laboratory-scale cells and large-scale PSMs have been devised.

Research on stability is bound to remain a crucial thematic focus in the field of PSCs as they are still a long distance away from practical applications, especially as commercialization will require a lifespan of over 10 years. It must also be noted that research on effective strategies for stability improvement of C-PSCs still lags behind efforts to boost efficiency, even though the relevant degradation mechanisms are well understood. To fabricate long-term stable C-PSCs, three aspects should be paid particular attention.

First, highly-stable, high-quality PVK materials should be extensively investigated. The range of thermal stress tolerance of each PVK material should be accurately measured to allow for appropriate selection of device fabrication process and encapsulation technique. Moreover, the development of stable spacer layers that can suppress the volatilization of organic components in PVK should also be

encouraged.

Second, with regards to the hydrophilic functional groups at lattice edges and at defects of carbon layers, the loose and porous network of carbon materials should be properly treated before using as CEs. To avoid degradation of PVK materials, few auxiliary solvents should be utilized in CEs during the deposition process.

Thirdly, due to the special properties of PVK materials, the commercial encapsulation techniques used for silicon and other organic thin-film photovoltaics are not suitable for C-PSCs. It is thus necessary to develop novel encapsulation techniques for large-scale carbon-based PSMs. Given the issue of recycling and reusing of large-scale PSMs in the future, development of the bio- or natural-degradable eco-friendly sealing materials is likely to become an important field of research.

Declaration of competing interest

None.

Acknowledgements

This work was financially supported by the National Natural Science Foundation of China (Grant No. 21703027, 51772039, 21903010, and 51972293). We extend our appreciation to the Supercomputing Center of Dalian University of Technology for providing access to the supercomputer.

Reference

[1] https://www.nrel.gov/pv/assets/pdfs/pv-efficiency-chart.20200406.pdf.

[2] S.D. Stranks, G.E. Eperon, G. Grancini, C. Menelaou, M.J.P. Alcocer, T. Leijtens, L. M. Herz, A. Petrozza, H. J. Snaith, Electron-hole diffusion lengths exceeding 1 micrometer in an organometal trihalide perovskite absorber, Science 342 (2013) 341-344. https://doi.org/10.1126/science.1243982.

[3] Y. Zhao, K. Zhu, Organic-inorganic hybrid lead halide perovskites for optoelectronic and electronic applications, Chem. Soc. Rev. 45 (2016) 655-689. https://doi.org/10.1039/C4CS00458B.

[4] G. Xing, N. Mathews, S. Sun, S.S. Lim, Y.M. Lam, M. Grätzel, S. Mhaisalkar, T.C. Sum, Long-range balanced electron- and hole-transport lengths in organic-inorganic $CH_3NH_3PbI_3$, Science 342 (2013) 344-347. https://doi.org/10.1126/science.1243167.

[5] J.A. Christians, P.A. Miranda Herrera, P.V. Kamat, Transformation of the excited state and photovoltaic efficiency of $CH_3NH_3PbI_3$ perovskite upon controlled exposure to humidified air, J. Am. Chem. Soc. 137 (2015) 1530-1538. https://doi.org/10.1021/ja511132a.

[6] T. Leijtens, E.T. Hoke, G. Grancini, D.J. Slotcavage, G.E. Eperon, J.M. Ball, M.D. Bastiani, A.R. Bowring, N. Martino, K. Wojciechowski, M.D. McGehee, H.J. Snaith, A. Petrozza, 2015. Mapping electric field-induced switchable poling and structural degradation in hybrid lead halide perovskite thin films. Adv. Energy Mater. 5, e1500962. https://doi.org/10.1002/aenm.201500962.
[7] J.M. Frost, K.T. Butler, F. Brivio, C.H. Hendon, M. van Schilfgaarde, A. Walsh, Atomistic origins of high-performance in hybrid halide perovskite solar cells, Nano Lett. 14 (2014) 2584-2590. https://doi.org/10.1021/nl500390f.
[8] N. Aristidou, I. Sanchez-Molina, T. Chotchuangchutchaval, M. Brown, L. Martinez, T. Rath, S.A. Haque, The role of cxygen in the degradation of methylammonium lead trihalide perovskite photoactive layers, Angew. Chem. Int. Ed. 54 (2015) 8208-8212. https://doi.org/10.1002/anie.201503153.
[9] N. Aristidou, C. Eames, I. Sanchez-Molina, X. Bu, J. Kosco, M.S. Islam, S.A. Haque, 2017. Fast oxygen diffusion and iodide defects mediate oxygen-induced degradation of perovskite solar cells. Nat. Commun. 8, e15218. https://doi.org/10.1038/ncomms15218.
[10] C.C. Boyd, R. Cheacharoen, T. Leijtens, M.D. McGehee, Understanding degradation mechanisms and improving stability of perovskite photovoltaics, Chem. Rev. 119 (2019) 3418-3451. https://doi.org/10.1021/acs.chemrev.8b00336.
[11] Z. Fan, H. Xiao, Y. Wang, Z. Zhao, Z. Lin, H.-C. Cheng, S.-J. Lee, G. Wang, Z. Feng, W. A. GoddardIII, Y. Huang, X. Duan, Layer-by-layer degradation of methylammonium lead tri-iodide perovskite microplates, Joule 1 (2017) 548-562. https://doi.org/10.1016/j.joule.2017.08.005.
[12] B. Charles, J. Dillon, O.J. Weber, M.S. Islam, M.T. Weller, Understanding the stability of mixed A-cation lead iodide perovskites, J. Mater. Chem. A 5 (2017) 22495-22499. https://doi.org/10.1039/C7TA08617B.
[13] K. Domanski, J.P. Correa-Baena, N. Mine, M.K. Nazeeruddin, A. Abate, M. Saliba, W. Tress, A. Hagfeldt, M. Grätzel, Not all that glitters is gold: metal-migration-induced degradation in perovskite solar cells, ACS Nano 10 (2016) 6306-6314. https://doi.org/10.1021/acsnano.6b02613.
[14] N.G. Park, 2019. Research direction toward scalable, stable, and high efficiency perovskite solar cells. Adv. Energy Mater. 10, e1903106. https://doi.org/10.1002/aenm.201903106.
[15] Z. Guo, L. Gao, C. Zhang, Z. Xu, T. Ma, Low-temperature processed non-TiO_2 electron selective layers for perovskite solar cells, J. Mater. Chem. A 6 (2018) 4572-4589. https://doi.org/10.1039/C7TA10742K.
[16] Q. Jiang, X. Zhang, J. You, 2018. SnO_2: A wonderful electron transport layer for perovskite solar cells. Small 14, e1801154. https://doi.org/10.1002/smll.201801154.
[17] Z. Zhao, F. Gu, H. Rao, S. Ye, Z. Liu, Z. Bian, C. Huang, 2019. Metal halide perovskite materials for solar cells with long-term stability. Adv. Energy Mater. 9, e1802671. https://doi.org/10.1002/aenm.201802671.
[18] J. Cao, F. Meng, L. Gao, S. Yang, Y. Yan, N. Wang, A. Liu, Y. Li, T. Ma, Alternative electrodes for HTMs and noble-metal-free perovskite solar cells: 2D MXenes electrodes, RSC Advances 9 (2019) 34152-34157. https://doi.org/10.1039/C9RA06091J.
[19] Z. Ku, Y. Rong, M. Xu, T. Liu, H. Han, 2013. Full printable processed mesoscopic $CH_3NH_3PbI_3/TiO_2$ heterojunction solar cells with carbon counter electrode. Sci. Rep. 3, e3132. https://doi.org/10.1038/srep03132.
[20] J. You, Z. Hong, Y. Yang, Q. Chen, M. Cai, T.-B. Song, C.-C. Chen, S. Lu, Y. Liu, H. Zhou, Y. Yang, Low-temperature solution-processed perovskite solar cells with high efficiency and flexibility,

ACS Nano 8 (2014) 1674-1680. https://doi.org/10.1021/nn406020d.
[21] Y. Shao, Q. Wang, Q. Dong, Y. Yuan, J. Huang, Vacuum-free laminated top electrode with conductive tapes for scalable manufacturing of efficient perovskite solar cells, Nano Energy 16 (2015) 47-53. https://doi.org/10.1016/j.nanoen.2015.06.010.
[22] Q. Jiang, X. Sheng, B. Shi, X. Feng, T. Xu, Nickel-cathoded perovskite solar cells, J. Phys. Chem. C 118 (2014) 25878-25883. https://doi.org/10.1021/jp506991x.
[23] H. Zhou, Y. Shi, Q. Dong, H. Zhang, Y. Xing, K. Wang, Y. Du, T. Ma, Hole-conductor-free, metal-electrode-free $TiO_2/CH_3NH_3PbI_3$ heterojunction solar cells based on a low-temperature carbon electrode, J. Phys. Chem. Lett. 5 (2014) 3241-3246. https://doi.org/10.1021/jz5017069.
[24] K. Aitola, K. Domanski, J.-P. Correa-Baena, K. Sveinbjörnsson, M. Saliba, A. Abate, M. Grätzel, E. Kauppinen, E.M.J. Johansson, W. Tress, A. Hagfeldt, G. Boschloo, 2017. High temperature-stable perovskite solar cell based on low-cost carbon nanotube hole contact. Adv. Mater. 29, e1606398. https://doi.org/10.1002/adma.201606398.
[25] S.N. Habisreutinger, R.J. Nicholas, H.J. Snaith, 2017. Carbon nanotubes in perovskite solar cells. Adv. Energy Mater. 7, e1601839. https://doi.org/10.1002/aenm.201601839.
[26] L. Fagiolari, F. Bella, Carbon-based materials for stable, cheaper and large-scale processable perovskite solar cells, Energy Environ. Sci. 12 (2019) 3437-3472. https://doi.org/10.1039/C9EE02115A.
[27] R. Hu, L. Chu, J. Zhang, X. Li, W. Huang, Carbon materials for enhancing charge transport in the advancements of perovskite solar cells, J. Power Sources 361 (2017) 259-275. https://doi.org/10.1016/j.jpowsour.2017.06.051.
[28] Y. Zhou, X. Yin, Q. Luo, X. Zhao, D. Zhou, J. Han, F. Hao, M. Tai, J. Li, P. Liu, K. Jiang, H. Lin, Efficiently improving the stability of inverted perovskite solar cells by employing polyethylenimine-modified carbon nanotubes as electrodes, ACS Appl. Mater. Interfaces 10 (2018) 31384-31393. https://doi.org/10.1021/acsami.8b10253.
[29] X. Meng, J. Zhou, J. Hou, X. Tao, S.H. Cheung, S.K. So, S. Yang, 2018. Versatility of carbon enables all carbon based perovskite solar cells to achieve high efficiency and high stability. Adv. Mater. 30, e1706975. https://doi.org/10.1002/adma.201706975.
[30] H. Zhang, J. Xiao, J. Shi, H. Su, Y. Luo, D. Li, H. Wu, Y.-B. Cheng, Q. Meng, 2018. Self-adhesive macroporous carbon electrodes for efficient and stable perovskite solar cells. Adv. Funct. Mater. 28, e1802985. https://doi.org/10.1002/adfm.201802985.
[31] G. Grancini, C. Roldan-Carmona, I. Zimmermann, E. Mosconi, X. Lee, D. Martineau, S. Narbey, F. Oswald, F. De Angelis, M. Graetzel, M.K. Nazeeruddin, 2017. One-year stable perovskite solar cells by 2D/3D interface engineering. Nat. Commun. 8, e15684. https://doi.org/10.1038/ncomms15684.
[32] Y. Cai, L. Liang, P. Gao, 2018. Promise of commercialization: Carbon materials for low-cost perovskite solar cells. Chin. Phys. B 27, e018805. https://doi.org/10.1088/1674-1056/27/1/018805.
[33] H. Chen, S. Yang, 2017. Carbon-based perovskite solar cells without hole transport materials: The front runner to the market?. Adv. Mater. 29, e1603994. https://doi.org/10.1002/adma.201603994.
[34] Z. Wu, T. Song, B. Sun, Carbon-based materials used for perovskite solar cells, Chemnanomat 3 (2017) 75-88. https://doi.org/10.1002/cnma.201600312.
[35] M. Wu, M. Sun, H. Zhou, J.Y. Ma, T. Ma, 2019. Carbon counter electrodes in dye-sensitized and perovskite solar cells. Adv. Funct. Mater. 30, e1906451. https://doi.org/10.1002/adfm.201906451.
[36] B. Xu, J. Huang, H. Agren, L. Kloo, A. Hagfeldt, L.C. Sun, AgTFSI as p-type dopant for efficient and stable solid-state dye-sensitized and perovskite solar cells, Chemsuschem 7 (2014) 3252-3256.

https://doi.org/10.1002/cssc.201402678.
[37] W.Z. Li, H.P. Dong, L.D. Wang, N. Li, X.D. Guo, J.W. Li, Y. Qiu, Montmorillonite as bifunctional buffer layer material for hybrid perovskite solar cells with protection from corrosion and retarding recombination, J. Mater. Chem. A 2 (2014) 13587-13592. https://doi.org/10.1039/C4TA01550A.
[38] N. Rolston, B.L. Watson, C.D. Bailie, M.D. McGehee, J.P. Bastos, R. Gehlhaar, J.-E. Kim, D. Vak, A.T. Mallajosyula, G.G. Aditya, D. Mohitee, R.H. Dauskardtb, Mechanical integrity of solution-processed perovskite solar cells, Extreme Mech. Lett. 9 (2016) 353-358. https://doi.org/10.1016/j.eml.2016.06.006.
[39] T.A. Berhe, W.-N. Su, C.-H. Chen, C.-J. Pan, J.-H. Cheng, H.-M. Chen, M.C. Tsai, L.-Y. Chen, A.A. Dubale, B.-J. Hwang, Organometal halide perovskite solar cells: degradation and stability, Energy Environ. Sci. 9 (2016) 323-356. https://doi.org/10.1039/C5EE02733K.
[40] T. Leijtens, G.E. Eperon, S. Pathak, A. Abate, M.M. Lee, H.J. Snaith, 2013. Overcoming ultraviolet light instability of sensitized TiO_2 with meso-superstructured organometal tri-halide perovskite solar cells. Nat. Commun. 4, e2885. https://doi.org/10.1038/ncomms3885.
[41] N.H. Nickel, F. Lang, V.V. Brus, O. Shargaieva, J. Rappich, 2017. Unraveling the light-induced degradation mechanisms of $CH_3NH_3PbI_3$ perovskite films. Adv. Electron. Mater. 3, e1700158. https://doi.org/10.1016/j.orgel.2019.01.005.
[42] Z. Li, M. Yang, J.-S. Park, S.-H. Wei, J.J. Berry, K. Zhu, Stabilizing perovskite structures by tuning tolerance factor: Formation of formamidinium and cesium lead iodide solid-state alloys, Chem. Mater. 28 (2016) 284-292. https://doi.org/10.1021/acs.chemmater.5b04107.
[43] R. Heiderhoff, T. Haeger, N. Pourdavoud, T. Hu, M. Al-Khafaji, A. Mayer, Y. Chen, H.-C. Scheer, T. Riedl, Thermal conductivity of methylammonium lead halide perovskite single crystals and thin films: A comparative study, J. Phys. Chem. C 121 (2017) 28306-28311. https://doi.org/10.1021/acs.jpcc.7b11495.
[44] A.K. Baranwal, H. Kanda, N. Shibayama, H. Masutani, T.A.N. Peiris, S. Kanaya, H. Segawa, T. Miyasaka, S. Ito, Thermal degradation analysis of sealed perovskite solar cell with porous carbon eectrode at 100 °C for 7000 h, Energy Technology 7 (2019) 245-252. https://doi.org/10.1002/ente.201800572.
[45] T. Malinauskas, D. Tomkute-Luksiene, R. Sens, M. Daskeviciene, R. Send, H. Wonneberger, V. Jankauskas, I. Bruder, V. Getautis, Enhancing thermal stability and lifetime of solid-state dye-sensitized solar cells via molecular engineering of the hole-transporting material spiro-OMeTAD, ACS Appl. Mater. Interfaces 7 (2015) 11107-11116. https://doi.org/10.1021/am5090385.
[46] W.Z. Li, H.P. Dong, L.D. Wang, N. Li, X.D. Guo, J.W. Li, Y. Qiu, Montmorillonite as bifunctional buffer layer material for hybrid perovskite solar cells with protection from corrosion and retarding recombination, J. Mater. Chem. A 2 (2014) 13587-13592. https://doi.org/10.1039/C4TA01550A.
[47] F. Matteocci, L. Cina, E. Lamanna, S. Cacovich, G. Divitini, P.A. Midgley, C. Ducati, A.D. Carlo, Encapsulation for long-term stability enhancement of perovskite solar cells, Nano Energy 30 (2016) 162-172. https://doi.org/10.1016/j.nanoen.2016.09.041.
[48] F. Bella, G. Griffini, J.-P. Correa-Baena, G. Saracco, M. Gratzel, A. Hagfeldt, S. Turri, C. Gerbaldi, Improving efficiency and stability of perovskite solar cells with photocurable fluoropolymers, Science 354 (2016) 203-206. https://doi.org/10.1126/science.aah4046.
[49] L. Shi, T. L. Young, J. Kim, Y. Sheng, L. Wang, Y. Chen, Z. Feng, M.J. Keevers, X. Hao, P.J. Verlinden, M.A. Green, A.W. Y. Ho-Baillie, Accelerated lifetime testing of organic-inorganic perovskite solar cells encapsulated by polyisobutylene, ACS Appl. Mater. Interfaces 9 (2017)

25073-25081. https://doi.org/10.1021/acsami.7b07625.
[50] Q. Wei, Z. Yang, D. Yang, W. Zi, X. Ren, Y. Liu, X. Liu, J. Feng, S.(Frank) Liu, The effect of transparent conductive oxide on the performance $CH_3NH_3PbI_3$ perovskite solar cell without electron/hole selective layers, Solar Energy 135 (2016) 654-661. https://doi.org/10.1016/j.solener.2016.06.044.
[51] W. Ke, G. Fang, J. Wan, H. Tao, Q. Liu, L. Xiong, P. Qin, J. Wang, H. Lei, G. Yang, M. Qin, X. Zhao, Y. Yan, 2015. Efficient hole-blocking layer-free planar halide perovskite thin-film solar cells. Nat. Commun. 6, e6700. https://doi.org/10.1038/ncomms7700.
[52] J. Zhou, J. Hou, X. Tao, X. Meng, S. Yang, Solution-processed electron transport layer of n-doped fullerene for efficient and stable all carbon based perovskite solar cells, J. Mater. Chem. A 7 (2019) 7710-7716. https://doi.org/10.1039/C9TA00118B.
[53] F. Meng, A. Liu, L. Gao, J. Cao, Y. Yan, N. Wang, M. Fan, G. Wei, T. Ma, Current progress in interfacial engineering of carbon-based perovskite solar cells, J. Mater. Chem. A 7 (2019) 8690-8699. https://doi.org/10.1039/C9TA01364D.
[54] H. Wei, J. Xiao, Y. Yang, S. Lv, J. Shi, X. Xu, J. Dong, Y. Luo, D. Li, Q. Meng, Free-standing flexible carbon electrode for highly efficient hole-conductor-free perovskite solar cells, Carbon 93 (2015) 861-868. https://doi.org/10.1016/j.carbon.2015.05.042.
[55] F. Meng, L. Gao, Y. Yan, J. Cao, N. Wang, T. Wang, T. Ma, Ultra-low-cost coal-based carbon electrodes with seamless interfacial contact for effective sandwich-structured perovskite solar cells, Carbon 145 (2019) 290-296. https://doi.org/10.1016/j.carbon.2019.01.047.
[56] C. Wang, F. Meng, T. Wang, T. Ma, J. Qiu, Monolithic coal-based carbon counter electrodes for highly efficient dye-sensitized solar cells, Carbon 67 (2014) 465-474. https://doi.org/10.1016/j.carbon.2013.10.019.
[57] C. Wang, F. Meng, M. Wu, X. Lin, T. Wang, J. Qiu, T. Ma, A low-cost bio-inspired integrated carbon counter electrode for high conversion efficiency dye-sensitized solar cells, Phys. Chem. Chem. Phys. 15 (2013) 14182-14187. https://doi.org/10.1039/C3CP52525B.
[58] H. Chen, S. Yang, High-quality perovskite in thick scaffold: a core issue for hole transport material-free perovskite solar cells, Science Bulletin 61 (2016) 1680-1688. https://doi.org/10.1007/s11434-016-1164-1.
[59] Z. Liu, S. Bi, G. Hou, C. Ying, X. Su, Dual-sized TiO_2 nanoparticles as scaffold layers in carbon-based mesoscopic perovskite solar cells with enhanced performance, J. Power Sources 430 (2019) 12-19. https://doi.org/10.1016/j.jpowsour.2019.05.005.
[60] W. Chen, X. Yin, M. Que, H. Xie, J. Liu, C. Yang, Y. Guo, Y. Wu, W. Que, A comparative study of planar and mesoporous perovskite solar cells with printable carbon electrodes, J. Power Sources 412 (2019) 118-124. https://doi.org/10.1016/j.jpowsour.2018.11.031.
[61] F. Zhang, X. Yang, H. Wang, M. Cheng, J. Zhao, L. Sun, Structure engineering of hole-conductor free perovskite-based solar cells with low-temperature-processed commercial carbon paste as cathode, ACS Appl. Mater. Interfaces 6 (2014) 16140-16146. https://doi.org/10.1021/am504175x.
[62] X. Zheng, Z. Wei, H. Chen, Q. Zhang, H. He, S. Xiao, Z. Fan, K. S. Wong, S. Yang, Designing nanobowl arrays of mesoporous TiO_2 as an alternative electron transporting layer for carbon cathode-based perovskite solar cells, Nanoscale 8 (2016) 6393-6402. https://doi.org/10.1039/C5NR06715D.
[63] J. Liu, L. Zhu, S. Xiang, H. Wang, H. Liu, W. Li, H. Chen, Cs-doped TiO_2 nanorod array enhances electron injection and transport in carbon-based $CsPbI_3$ perovskite solar cells, ACS Sustainable Chem.

Eng. 7 (2019) 16927-16932. https://doi.org/10.1021/acssuschemeng.9b04772.
[64] C.S. Ponseca, Jr., T.J. Savenije, M. Abdellah, K. Zheng, A. Yartsev, T. Pascher, T. Harlang, P. Chabera, T. Pullerits, A. Stepanov, J.-P. Wolf, V. Sundström, Organometal halide perovskite solar cell materials rationalized: Ultrafast charge generation, high and microsecond-long balanced mobilities, and slow recombination, J. Am. Chem. Soc. 136 (2014) 5189-5192. https://doi.org/10.1021/ja412583t.
[65] A.F.C. Emma Carter, Damien M. Murphy, Evidence for O_2^- radical stabilization at surface oxygen vacancies on polycrystalline TiO_2, J. Phys. Chem. C 111 (2007) 10630-10638. https://doi.org/10.1021/jp0729516.
[66] J.H. Heo, S.H. Im, J.H. Noh, T.N. Mandal, C.S. Lim, J.A. Chang, Y.H. Lee, H. Kim, A. Sarkar, M.K. Nazeeruddin, M. Grätzel, S. Il Seok, Efficient inorganic-organic hybrid heterojunction solar cells containing perovskite compound and polymeric hole conductors, Nat. Photonics 7 (2013) 487-492. https://doi.org/10.1038/nphoton.2013.80.
[67] P.-W. Liang, C.-C. Chueh, S.T. Williams, A.K.Y. Jen, 2015. Roles of fullerene-based interlayers in enhancing the performance of organometal perovskite thin-film solar cells. Adv. Energy Mater. 5, e1402321. https://doi.org/10.1002/aenm.201402321.
[68] H. Yoon, S.M. Kang, J.-K. Lee, M. Choi, Hysteresis-free low-temperature-processed planar perovskite solar cells with 19.1% efficiency, Energy Environ. Sci. 9 (2016) 2262-2266. https://doi.org/10.1039/C6EE01037G.
[69] J. Yoon, H. Sung, G. Lee, W. Cho, N. Ahn, H.S. Jung, M. Choi, Superflexible, high-efficiency perovskite solar cells utilizing graphene electrodes: towards future foldable power sources, Energy Environ. Sci. 10 (2017) 337-345. https://doi.org/10.1039/C6EE02650H.
[70] P. Topolovsek, F. Lamberti, T. Gatti, A. Cito, J.M. Ball, E. Menna, C. Gadermaier, A. Petrozza, Functionalization of transparent conductive oxide electrode for TiO_2-free perovskite solar cells, J. Mater. Chem. A 5 (2017) 11882-11893. https://doi.org/10.1039/C7TA02405C.
[71] N. Ahn, I. Jeon, J. Yoon, E.I. Kauppinen, Y. Matsuo, S. Maruyama, M. Choi, Carbon-sandwiched perovskite solar cell, J. Mater. Chem. A 6 (2018) 1382-1389. https://doi.org/10.1039/C7TA09174E.
[72] T. Gatti, E. Menna, M. Meneghetti, M. Maggini, A. Petrozza, F. Lamberti, The renaissance of fullerenes with perovskite solar cells, Nano Energy 41 (2017) 84-100. https://doi.org/10.1016/j.nanoen.2017.09.016.
[73] S. Collavini, J. L. Delgado, Fullerenes: the stars of photovoltaics, Sustainable Energy Fuels 2 (2018) 2480-2493. https://doi.org/10.1039/C8SE00254A.
[74] Q. Zhang, C.S. Dandeneau, X. Zhou, G. Cao, 2009. ZnO nanostructures for dye-sensitized solar cells. Adv. Mater. 21, 4087-4108. https://doi.org/10.1002/adma.200803827.
[75] J. Zhang, E. Jose Juarez-Perez, I. Mora-Sero, B. Viana, T. Pauporte, Fast and low temperature growth of electron transport layers for efficient perovskite solar cells, J. Mater. Chem. A 3 (2015) 4909-4915. https://doi.org/10.1039/C4TA06416J.
[76] M.A. Mahmud, N.K. Elumalai, M.B. Upama, D. Wang, K.H. Chan, M. Wright, C. Xu, F. Haque, A. Uddin, Low temperature processed ZnO thin film as electron transport layer for efficient perovskite solar cells, Sol. Energ. Mater. Sol. C. 159 (2017) 251-264. https://doi.org/10.1016/j.solmat.2016.09.014.
[77] H. Zhou, Y. Shi, K. Wang, Q. Dong, X. Bai, Y. Xing, Y. Du, T. Ma, Low-Temperature Processed and Carbon-Based ZnO/$CH_3NH_3PbI_3$/C Planar Heterojunction Perovskite Solar Cells, J. Phys. Chem. C 119 (2015) 4600-4605. https://doi.org/10.1021/jp512101d.
[78] M. Shirazi, M.R. Toroghinejad, R. Sabet Dariani, M.T. Hosseinnejad, Fabrication of

hole-conductor-free perovskite solar cells based on Al doped ZnO and low-cost carbon electrode, J. Mater. Sci.-Mater. El. 29 (2018) 10092-100101. https://doi.org/10.1007/s10854-018-9054-8.
[79] M. Yang, J. Li, J. Li, Z. Yuan, J. Zou, G. Lei, L. Zhao, X. Wang, B. Dong, S. Wang, High efficient and long-time stable planar heterojunction perovskite solar cells with doctor-bladed carbon electrode, J. Power Sources 424 (2019) 61-67. https://doi.org/10.1016/j.jpowsour.2019.03.092.
[80] S. Lin, B. Yang, X. Qiu, J. Yan, J. Shi, Y. Yuan, W. Tan, X. Liu, H. Huang, Y. Gao, C. Zhou, Efficient and stable planar hole-transport-material-free perovskite solar cells using low temperature processed SnO_2 as electron transport material, Org. Electron. 53 (2018) 235-241. https://doi.org/10.1016/j.orgel.2017.12.002.
[81] Y. Qiang, J. Cheng, Y. Qi, H. Shi, H. Liu, C. Geng, Y. Xie, 2019. Low-temperature preparation of HTM-free SnO_2-based planar heterojunction perovskite solar cells with commercial carbon as counter electrode. J. Alloy. Compd. 809, e151817. https://doi.org/10.1016/j.jallcom.2019.151817.
[82] X. Dou, D. Sabba, N. Mathews, L. H. Wong, Y. M. Lam, S. Mhaisalkar, Hydrothermal synthesis of high electron mobility Zn-doped SnO_2 nanoflowers as photoanode material for efficient dye-sensitized solar cells, Chem. Mater. 23 (2011) 3938-3945. https://doi.org/10.1021/cm201366z.
[83] H. Ye, Z. Liu, X. Liu, B. Sun, X. Tan, Y. Tu, T. Shi, Z. Tang, G. Liao, 17.78% efficient low-temperature carbon-based planar perovskite solar cells using Zn-doped SnO_2 electron transport layer, Appl. Surf. Sci. 478 (2019) 417-425. https://doi.org/10.1016/j.apsusc.2019.01.237.
[84] Z. Guo, S. Teo, Z. Xu, C. Zhang, Y. Kamata, S. Hayase, T. Ma, Achievable high V_{oc} of carbon based all-inorganic $CsPbIBr_2$ perovskite solar cells through interface engineering, J. Mater. Chem. A 7 (2019) 1227-1232. https://doi.org/10.1039/C8TA09838G.
[85] D. Shen, W. Zhang, Y. Li, A. Abate, M. Wei, Facile Deposition of Nb_2O_5 thin film as an electron-transporting layer for highly efficient perovskite solar cells, ACS Appl. Nano Mater. 1 (2018) 4101-4109. https://doi.org/10.1021/acsanm.8b00859.
[86] Y. Guo, J. Tao, J. Jiang, J. Zhang, J. Yang, S. Chen, J. Chu, Low temperature solution deposited niobium oxide films as efficient electron transport layer for planar perovskite solar cell, Sol. Energ. Mater. Sol. C. 188 (2018) 66-72. https://doi.org/10.1016/j.solmat.2018.08.020.
[87] F. Zhao, Y. Guo, X. Wang, J. Tao, J. Jiang, Z. Hu, J. Chu, Enhanced performance of carbon-based planar $CsPbBr_3$ perovskite solar cells with room-temperature sputtered Nb_2O_5 electron transport layer, Solar Energy 191 (2019) 263-271. https://doi.org/10.1016/j.solener.2019.08.069.
[88] A. Mei, X. Li, L. Liu, Z. Ku, T. Liu, Y. Rong, M. Xu, M. Hu, J. Chen, Y. Yang, M. Grätzel, H. Han, A hole-conductor-free, fully printable mesoscopic perovskite solar cell with high stability, Science 345 (2014) 295-298. https://doi.org/10.1126/science.1254763.
[89] Q.-Q. Chu, B. Ding, Q. Qiu, Y. Liu, C.-X. Li, C.-J. Li, G.-J. Yang, B. Fang, Cost effective perovskite solar cells with a high efficiency and open-circuit voltage based on a perovskite-friendly carbon electrode, J. Mater. Chem. A 6 (2018) 8271-8279. https://doi.org/10.1039/C7TA10871K.
[90] E.V. Péan, C.S. De Castro, S. Dimitrov, F. De Rossi, S. Meroni, J. Baker, T. Watson, M.L. Davies, 2020. Investigating the superoxide formation and stability in mesoporous carbon perovskite solar cells with an aminovaleric acid additive. Adv. Funct. Mater. 30, e1909839. https://doi.org/10.1002/adfm.201909839.
[91] Y. Hu, S. Si, A. Mei, Y. Rong, H. Liu, X. Li, H. Han, 2017. Stable large-area (10×10 cm^2) printable mesoscopic perovskite module exceeding 10% efficiency. Solar RRL 1, e1600019. https://doi.org/10.1002/solr.201600019.
[92] L. Zhang, T. Liu, L. Liu, M. Hu, Y. Yang, A. Mei, H. Han, The effect of carbon counter electrodes

on fully printable mesoscopic perovskite solar cells, J. Mater. Chem. A 3 (2015) 9165-9170. https://doi.org/10.1039/C4TA04647A.
[93] T. Liu, L. Liu, M. Hu, Y. Yang, L. Zhang, A. Mei, H. Han, Critical parameters in TiO_2/ZrO_2/Carbon-based mesoscopic perovskite solar cell, J. Power Sources 293 (2015) 533-538. https://doi.org/10.1016/j.jpowsour.2015.05.106.
[94] Y. Yang, K. Ri, A. Mei, L. Liu, M. Hu, T. Liu, X. Li, H. Han, The size effect of TiO_2 nanoparticles on a printable mesoscopic perovskite solar cell, J. Mater. Chem. A 3 (2015) 9103-9107. https://doi.org/10.1039/C4TA07030E.
[95] J. Chen, Y. Xiong, Y. Rong, A. Mei, Y. Sheng, P. Jiang, Y. Hu, X. Li, H. Han, Solvent effect on the hole-conductor-free fully printable perovskite solar cells, Nano Energy 27 (2016) 130-137. https://doi.org/10.1016/j.nanoen.2016.06.047.
[96] X. Hou, Y. Hu, H. Liu, A. Mei, X. Li, M. Duan, G. Zhang, Y. Rong, H. Han, Effect of guanidinium on mesoscopic perovskite solar cells, J. Mater. Chem. A 5 (2017) 73-78. https://doi.org/10.1039/C6TA08418D.
[97] Y. Rong, X. Hou, Y. Hu, A. Mei, L. Liu, P. Wang, H. Han, 2017. Synergy of ammonium chloride and moisture on perovskite crystallization for efficient printable mesoscopic solar cells. Nat. Commun. 8, e14555. https://doi.org/10.1038/ncomms14555.
[98] M. Hu, L. Liu, A. Mei, Y. Yang, T. Liu, H. Han, Efficient hole-conductor-free, fully printable mesoscopic perovskite solar cells with a broad light harvester $NH_2CH_2NH_2PbI_3$, J. Mater. Chem. A 2 (2014) 17115-17121. https://doi.org/10.1039/C4TA03741C.
[99] X. Li, M. Tschumi, H. Han, S.S. Babkair, R.A. Alzubaydi, A.A. Ansari, S.S. Habib, M.K. Nazeeruddin, S.M. Zakeeruddin, M. Grätzel, Outdoor performance and stability under elevated temperatures and long-term light soaking of triple-Layer mesoporous perovskite photovoltaics, Energy Technology 3 (2015) 551-555. https://doi.org/10.1002/ente.201500045.
[100] S.G. Hashmi, D. Martineau, X. Li, M. Ozkan, A. Tiihonen, M.I. Dar, T. Sarikka, S. M. Zakeeruddin, J. Paltakari, P.D. Lund, M. Grätzel, 2017. Air processed inkjet infiltrated carbon based printed perovskite solar cells with high stability and reproducibility. Adv. Mater. Technol. 2, e1600183. https://doi.org/10.1002/admt.201600183.
[101] A. Pockett, D. Raptis, S.M.P. Meroni, J. Baker, T. Watson, M. Carnie, Origin of exceptionally slow light soaking effect in mesoporous carbon perovskite solar cells with AVA additive, J. Phys. Chem. C 123 (2019) 11414-11421. https://doi.org/10.1021/acs.jpcc.9b01058.
[102] C.-T. Lin, F. De Rossi, J. Kim, J. Baker, J. Ngiam, B. Xu, S. Pont, N. Aristidou, S.A. Haque, T. Watson, M.A. McLachlan, J. R. Durrant, Evidence for surface defect passivation as the origin of the remarkable photostability of unencapsulated perovskite solar cells employing aminovaleric acid as a processing additive, J. Mater. Chem. A 7 (2019) 3006-3011. https://doi.org/10.1039/C8TA11985F.
[103] C. Xu, Z. Zhang, Y. Hu, Y. Sheng, P. Jiang, H. Han, J. Zhang, Printed hole-conductor-free mesoscopic perovskite solar cells with excellent long-term stability using PEAI as an additive, J. Energy Chem. 27 (2018) 764-768. https://doi.org/10.1016/j.jechem.2018.01.030.
[104] D. Papadatos, D. Sygkridou, E. Stathatos, 2020. Carbon-based, novel triple cation mesoscopic perovskite solar cell fabricated entirely under ambient air conditions. Mater. Lett. 268, e127621. https://doi.org/10.1016/j.matlet.2020.127621.
[105] H. Liu, W. Fu, B. Zong, L. Huang, B. Zhang, S. Wang, Z. Guo, H. Bala, G. Sun, J. Cao, Z. Zhan, A high stability, hole-conductor-free mixed organic cation pervoskite solar cells based on carbon counter electrode, Electrochim. Acta 266 (2018) 78-85. https://doi.org/10.1016/j.electacta.2018.02.007.

[106] B. Zong, W. Fu, H. Liu, L. Huang, H. Bala, X. Wang, G. Sun, J. Cao, Z. Zhang, Highly stable hole-conductor-free $CH_3NH_3Pb(I_{1-x}Br_x)_3$ perovskite solar cells with carbon counter electrode, J. Alloy. Compd. 748 (2018) 1006-1012. https://doi.org/10.1016/j.jallcom.2018.03.236.
[107] H. Zhang, H. Wang, S.T. Williams, D. Xiong, W. Zhang, C.C. Chueh, W. Chen, A.K.-Y. Jen, 2017. $SrCl_2$ Derived perovskite facilitating a high efficiency of 16% in hole-conductor-free fully printable mesoscopic perovskite solar cells. Adv. Mater. 29, e1606608. https://doi.org/10.1002/adma.201606608.
[108] S. Liu, W. Huang, P. Liao, N. Pootrakulchote, H. Li, J. Lu, J. Li, F. Huang, X. Shai, X. Zhao, Y. Shen, Y.-B. Cheng, M. Wang, 17% efficient printable mesoscopic PIN metal oxide framework perovskite solar cells using cesium-containing triple cation perovskite, J. Mater. Chem. A 5 (2017) 22952-22958. https://doi.org/10.1039/C7TA07660F.
[109] H. Chen, Z. Wei, X. Zheng, S. Yang, A scalable electrodeposition route to the low-cost, versatile and controllable fabrication of perovskite solar cells, Nano Energy 15 (2015) 216-226. https://doi.org/10.1016/j.nanoen.2015.04.025.
[110] X. Chang, W. Li, H. Chen, L. Zhu, H. Liu, H. Geng, , S. Xiang, J. Liu, X. Zheng, Y. Yang, S. Yang, Colloidal precursor-induced growth of ultra-even $CH_3NH_3PbI_3$ for high-performance paintable carbon-based perovskite solar cells, ACS Appl. Mater. Interfaces 8 (2016) 30184-30192. https://doi.org/10.1021/acsami.6b09925.
[111] H. Chen, X. Zheng, Q. Li, Y. Yang, S. Xiao, C. Hu, Y. Bai, T. Zhang, K.S. Wong, S. Yang, An amorphous precursor route to the conformable oriented crystallization of $CH_3NH_3PbBr_3$ in mesoporous scaffolds: toward efficient and thermally stable carbon-based perovskite solar cells, J. Mater. Chem. A 4 (2016) 12897-12912. https://doi.org/10.1039/C6TA06115J.
[112] J. Liu, Q. Zhou, N.K. Thein, L. Tian, D. Jia, E.M.J. Johansson, X. Zhang, In situ growth of perovskite stacking layers for high-efficiency carbon-based hole conductor free perovskite solar cells, J. Mater. Chem. A 7 (2019) 13777-13786. https://doi.org/10.1039/C9TA02772F.
[113] M. Saliba, T. Matsui, J.Y. Seo, K. Domanski, J.P. Correa-Baena, M.K. Nazeeruddin, S.M. Zakeeruddin, W. Tress, A. Abate, A, Hagfeldtd, M. Grätzel, Cesium-containing triple cation perovskite solar cells: improved stability, reproducibility and high efficiency, Energy Environ. Sci. 9 (2016) 1989-1997. https://doi.org/10.1039/C5EE03874J.
[114] B. Conings, J. Drijkoningen, N. Gauquelin, A. Babayigit, J. D'Haen, L. D'Olieslaeger, A. Ethirajan, J. Verbeeck, J. Manca, E. Mosconi, F.D. Angelis, H.-G. Boyen, 2015. Intrinsic thermal instability of methylammonium lead trihalide perovskite. Adv. Energy Mater. 5, e1500477. https://doi.org/10.1002/aenm.201500477.
[115] J. Zhou, J. Wu, N. Li, X. Li, Y.-Z. Zheng, X. Tao, Efficient all-air processed mixed cation carbon-based perovskite solar cells with ultra-high stability, J. Mater. Chem. A 7 (2019) 17594-17603. https://doi.org/10.1039/C9TA05744G.
[116] H. Li, S. Yang, S. Gong, J. Wu, S. Pan, Z. Chen, Q. Zhao, C. Shoud, Q. Shen, Perovskite films with a sacrificial cation for solar cells with enhanced stability based on carbon electrodes, J. Alloy. Compd. 797 (2019) 811-819. https://doi.org/10.1016/j.jallcom.2019.05.148.
[117] Z. Wu, Z. Liu, Z. Hu, Z. Hawash, L. Qiu, Y. Jiang, L.K. Ono, Y. Qi, 2019. Highly efficient and stable perovskite solar cells via modification of energy levels at the perovskite/carbon electrode interface. Adv. Mater. 31, e1804284. https://doi.org/10.1002/adma.201804284.
[118] C. Wang, J. Zhang, L. Jiang, L. Gong, H. Xie, Y. Gao, H. He, Z. Fang, J. Fan, Z. Chao, 2020. All-inorganic, hole-transporting-layer-free, carbon-based $CsPbIBr_2$ planar solar cells with ZnO as

electron-transporting materials. J. Alloy. Compd. 817, e152768. https://doi.org/10.1016/j.jallcom.2019.152768.
[119] S. Xiang, W. Li, Y. Wei, J. Liu, H. Liu, L. Zhu, S. Yang, H. Chen, Natrium doping pushes the efficiency of carbon-based $CsPbI_3$ perovskite solar cells to 10.7%, iScience 15 (2019) 156-164. https://doi.org/10.1016/j.isci.2019.04.025.
[120] J. Zhou, Z. Ye, J. Hou, J. Wu, Y.-Z. Zheng, X. Tao, Efficient ambient-air-stable HTM-free carbon-based perovskite solar cells with hybrid 2D–3D lead halide photoabsorbers, J. Mater. Chem. A 6 (2018) 22626-22635. https://doi.org/10.1039/C8TA07836J.
[121] H. Chen, S. Yang, Methods and strategies for achieving high-performance carbon-based perovskite solar cells without hole transport materials, J. Mater. Chem. A 7 (2019) 15476-15490. https://doi.org/10.1039/C9TA04707G.
[122] X. Wu, L. Xie, K. Lin, J. Lu, K. Wang, W. Feng, B. Fan, P. Yin, Z. Wei, Efficient and stable carbon-based perovskite solar cells enabled by the inorganic interface of CuSCN and carbon nanotubes, J. Mater. Chem. A 7 (2019) 12236-12243. https://doi.org/10.1039/C9TA02014D.
[123] X. Xu, Z. Liu, Z. Zuo, M. Zhang, Z. Zhao, Y. Shen, H. Zhou, Q. Chen, Y. Yang, M. Wang, Hole selective NiO contact for efficient perovskite solar cells with carbon electrode, Nano Lett. 15 (2015) 2402-2408. https://doi.org/10.1021/nl504701y.
[124] K. Cao, Z. Zuo, J. Cui, Y. Shen, T. Moehl, S.M. Zakeeruddin, M. Grätzel, M. Wang, Efficient screen printed perovskite solar cells based on mesoscopic TiO_2/Al_2O_3/NiO/carbon architecture, Nano Energy 17 (2015) 171-179. https://doi.org/10.1016/j.nanoen.2015.08.009.
[125] Z. Liu, A. Zhu, F. Cai, L. Tao, Y. Zhou, Z. Zhao, Q. Chen, Y.-B. Cheng, H. Zhou, Nickel oxide nanoparticles for efficient hole transport in p-i-n and n-i-p perovskite solar cells, J. Mater. Chem. A 5 (2017) 6597-6605. https://doi.org/10.1039/C7TA01593C.
[126] J. Cao, H. Yu, S. Zhou, M. Qin, T.-K. Lau, X. Lu, N. Zhao, C.-P. Wong, Low-temperature solution-processed NiO_x films for air-stable perovskite solar cells, J. Mater. Chem. A 5 (2017) 11071-11077. https://doi.org/10.1039/C7TA02228J.
[127] K. Yao, F. Li, Q. He, X. Wang, Y. Jiang, H. Huang, A. K.-Y. Jen, A copper-doped nickel oxide bilayer for enhancing efficiency and stability of hysteresis-free inverted mesoporous perovskite solar cells, Nano Energy 40 (2017) 155-162. https://doi.org/10.1016/j.nanoen.2017.08.014.
[128] Y. Wu, X. Yang, W. Chen, Y. Yue, M. Cai, F. Xie, E. Bi, A. Islam, L. Han, 2016. Perovskite solar cells with 18.21% efficiency and area over 1 cm^2 fabricated by heterojunction engineering. Nat. Energy 1, e16148. https://doi.org/10.1038/nenergy.2016.148.
[129] A. Bashir, J.H. Lew, S. Shukla, D. Gupta, T. Baikie, S. Chakraborty, R. Patidar, A. Bruno, S. Mhaisalkar, Z. Akhter, Cu-doped nickel oxide interface layer with nanoscale thickness for efficient and highly stable printable carbon-based perovskite solar cell, Solar Energy 182 (2019) 225-236. https://doi.org/10.1016/j.solener.2019.02.056.
[130] F. Behrouznejad, C.M. Tsai, S. Narra, E.W. Diau, N. Taghavinia, Interfacial investigation on printable carbon-based mesoscopic perovskite solar cells with NiO_x/C back electrode, ACS Appl. Mater. Interfaces 9 (2017) 25204-25215. https://doi.org/10.1021/acsami.7b02799.
[131] A. Singh, S.L.Y. Chang, R.K. Hocking, U. Bach, L. Spiccia, Highly active nickel oxide water oxidation catalysts deposited from molecular complexes, Energy Environ. Sci. 6 (2013) 579-586. https://doi.org/10.1039/C2EE23862D.
[132] M. Gong, W. Zhou, M.C. Tsai, J. Zhou, M. Guan, M.C. Lin, B. Zhang, Y. Hu, D.-Y. Wang, J. Yang, S.J. Pennycook, B.-J. Hwang, H. Dai, 2014. Nanoscale nickel oxide/nickel heterostructures for

active hydrogen evolution electrocatalysis. Nat. Commun 5, e4695. https://doi.org/10.1038/ncomms5695.
[133] P. Jiang, Y. Xiong, M. Xu, A. Mei, Y. Sheng, L. Hong, , T.W. Jones, G.J. Wilson, S. Xiong, D. Li, Y. Hu, Y. Rong, H. Han, The influence of the work function of hybrid carbon electrodes on printable mesoscopic perovskite solar cells, J. Phys. Chem. C 122 (2018) 16481-16487. https://doi.org/10.1021/acs.jpcc.8b02163.
[134] A. Bashir, S. Shukla, J.H. Lew, S. Shukla, A. Bruno, D. Gupta, T. Baikie, R. Patidar, Z. Akhter, A. Priyadarshi, N. Mathews, S.G. Mhaisalkar, Spinel Co_3O_4 nanomaterials for efficient and stable large area carbon-based printed perovskite solar cells, Nanoscale 10 (2018) 2341-2350. https://doi.org/10.1039/C7NR08289D.
[135] S. Gholipour, J.-P. Correa-Baena, K. Domanski, T. Matsui, L. Steier, F. Giordano, F. Tajabadi, W. Tress, M. Saliba, A. Abate, A. M. Ali, N. Taghavinia, M. Grätzel, A. Hagfeldt, 2016. Highly efficient and stable perovskite solar cells based on a low-cost carbon cloth. Adv. Energy Mater. 6, e1601116. https://doi.org/10.1002/aenm.201601116.
[136] S.N. Habisreutinger, T. Leijtens, G.E. Eperon, S.D. Stranks, R.J. Nicholas, H.J. Snaith, Carbon nanotube/polymer composites as a highly stable hole collection layer in perovskite solar cells, Nano Lett. 14 (2014) 5561-5568. https://doi.org/10.1021/nl501982b.
[137] G.-W. Kim, G. Kang, M.M. Byranvand, G.-Y. Lee, T. Park, Gradated mixed hole transport layer in a perovskite solar cell: Improving moisture stability and efficiency, ACS Appl. Mater. Interfaces 9 (2017) 27720-27726. https://doi.org/10.1021/acsami.7b07071.
[138] A. Rodrigues, M.C.R. Castro, A.S.F. Farinha, M. Oliveira, J.P.C. Tome, A.V. Machado, M.M. M.Raposo, L. Hilliou, G. Bernardo, Thermal stability of P3HT and P3HT:PCBM blends in the molten state, Polymer Testing 32 (2013) 1192-1201. https://doi.org/10.1016/j.polymertesting.2013.07.008.
[139] Z. Xiaoli, C. Haining, W. Zhanhua, Y. Yinglong, L. He, Y. Shihe, High-performance, stable and low-cost mesoscopic perovskite ($CH_3NH_3PbI_3$) solar cells based on poly(3-hexylthiophene)-modified carbon nanotube cathodes, Frontiers of Optoelectronics 9 (2016) 71-80. https://doi.org/10.1007/s12200-016-0566-7.
[140] Q.-Q. Chu, B. Ding, J. Peng, H. Shen, X. Li, Y. Liu, C.-X. Li, C.-J. Li, G.-J. Yang, T. P. White, K.R.Catchpole, Highly stable carbon-based perovskite solar cell with a record efficiency of over 18% via hole transport engineering, J. Mater. Sci. Technol. 35 (2019) 987-993. https://doi.org/10.1016/j.jmst.2018.12.025Get.
[141] M. Urbani, G. de la Torre, M.K. Nazeeruddin, T. Torres, Phthalocyanines and porphyrinoid analogues as hole- and electron-transporting materials for perovskite solar cells, Chem. Soc. Rev. 48 (2019) 2738-2766. https://doi.org/10.1039/C9CS00059C.
[142] F. Zhang, X. Yang, M. Cheng, W. Wang, L. Sun, Boosting the efficiency and the stability of low cost perovskite solar cells by using CuPc nanorods as hole transport material and carbon as counter electrode, Nano Energy 20 (2016) 108-116. https://doi.org/10.1016/j.nanoen.2015.11.034.
[143] Z. Liu, B. Sun, X. Liu, J. Han, H. Ye, T. Shi, Z. Tang, G. Liao, Efficient carbon-based $CsPbBr_3$ inorganic perovskite solar cells by using Cu-Phthalocyanine as hole transport material, Nanomicro-Lett. 10 (2018) 34. https://doi.org/10.1007/s40820-018-0187-3.
[144] X. Liu, Z. Liu, B. Sun, X. Tan, H. Ye, Y. Tu, T. Shi, Z. Tang, G. Liao, 17.46% efficient and highly stable carbon-based planar perovskite solar cells employing Ni-doped rutile TiO_2 as electron transport layer, Nano Energy 50 (2018) 201-211. https://doi.org/10.1016/j.nanoen.2018.05.031.
[145] B. Gil, A.J. Yun, Y. Lee, J. Kim, B. Lee, B. Park, Recent progress in inorganic hole transport

materials for efficient and stable perovskite solar cells, Electron. Mater. Lett. 15 (2019) 505-524. https://doi.org/10.1007/s13391-019-00163-6.
[146] S. Mashhoun, Y. Hou, H. Chen, F. Tajabadi, N. Taghavinia, H.-J. Egelhaaf, C.J. Brabec,2018. Resolving a critical instability in perovskite solar cells by designing a scalable and printable carbon based electrode-interface architecture. Adv. Energy Mater. 8, e1802085. https://doi.org/10.1002/aenm.201802085.
[147] N. Arora, M.I. Dar, S. Akin, R. Uchida, T. Baumeler, Y. Liu, S.M. Zakeeruddin, M. Grätzel,2019. Low-cost and highly efficient carbon-based perovskite solar cells exhibiting excellent long-term operational and UV stability. Small 15, e1904746. https://doi.org/10.1002/smll.201904746.
[148] Y. Yang, N.D. Pham, D. Yao, L. Fan, M.T. Hoang, V.T. Tiong, Z. Wang, H. Zhu, H. Wang, Interface engineering to eliminate hysteresis of carbon-based planar heterojunction perovskite solar cells via CuSCN incorporation, ACS Appl. Mater. Interfaces 11 (2019) 28431-28441. https://doi.org/10.1021/acsami.9b07318.
[149] R. Hu, R. Zhang, Y. Ma, W. Liu, L. Chu, W. Mao, J. Zhang, J. Yang, Y. Pu, X. Li, Enhanced hole transfer in hole-conductor-free perovskite solar cells via incorporating CuS into carbon electrodes, Appl. Surf. Sci. 462 (2018) 840-846. https://doi.org/10.1016/j.apsusc.2018.08.078.
[150] S. Sajid, A.M. Elseman, D. Wei, J. Ji, S. Dou, H. Huang, P. Cui, M. Li, NiO@carbon spheres: A promising composite electrode for scalable fabrication of planar perovskite solar cells at low cost, Nano Energy 55 (2019) 470-476. https://doi.org/10.1016/j.nanoen.2018.11.004.
[151] C. Cai, K. Zhou, H. Guo, Y. Pei, Z. Hu, J. Zhang, Y. Zhu, Enhanced hole extraction by NiO nanoparticles in carbon-based perovskite solar cells, Electrochim. Acta 312 (2019) 100-108. https://doi.org/10.1016/j.electacta.2019.04.191.
[152] Z. Wei, H. Chen, K. Yan, X. Zheng, S. Yang, Hysteresis-free multi-walled carbon nanotube-based perovskite solar cells with a high fill factor, J. Mater. Chem. A 3 (2015) 24226-24231. https://doi.org/10.1039/C5TA07714A.
[153] C. Tian, A. Mei, S. Zhang, H. Tian, S. Liu, F. Qin, Y. Xiong, Y. Rong, Y. Hu, Y. Zhou, S. Xie, H. Han, Oxygen management in carbon electrode for high-performance printable perovskite solar cells, Nano Energy 53 (2018) 160-167. https://doi.org/10.1016/j.nanoen.2018.08.050.
[154] P. Jiang, T.W. Jones, N.W. Duffy, K.F. Anderson, R. Bennett, M. Grigore, P. Marvig, Y. Xiong, T. Liu, Y. Sheng, L. Hong, X. Hou, M. Duan, Y. Hu, Y. Rong, G.J. Wilson, H. Han, Fully printable perovskite solar cells with highly-conductive, low-temperature, perovskite-compatible carbon electrode, Carbon 129 (2018) 830-836. https://doi.org/10.1016/j.carbon.2017.09.008.
[155] X. Zheng, H. Chen, Q. Li, Y. Yang, Z. Wei, Y. Bai, Y. Qiu, D. Zhou, K.S. Wong, S. Yang, Boron doping of multiwalled carbon nanotubes significantly enhances hole extraction in carbon-based perovskite solar cells, Nano Lett. 17 (2017) 2496-2505. https://doi.org/10.1021/acs.nanolett.7b00200.
[156] S.S. Mali, H. Kim, J.V. Patil, C.K. Hong, Bio-inspired carbon hole transporting layer derived from aloe vera plant for cost-effective fully printable mesoscopic carbon perovskite solar cells, ACS Appl. Mater. Interfaces 10 (2018) 31280-31290. https://doi.org/10.1021/acsami.8b08383.
[157] Z. Li, S.A. Kulkarni, P.P. Boix, E. Shi, A. Cao, K. Fu, S.K. Batabyal, J. Zhang, Q. Xiong, L. H. Wong, N. Mathews, S.G. Mhaisalkar, Laminated carbon nanotube networks for metal electrode-free efficient perovskite solar cells, ACS Nano 8 (2014) 6797-6804. https://doi.org/10.1021/nn501096h.
[158] P. You, Z. Liu, Q. Tai, S. Liu, F. Yan, Efficient semitransparent perovskite solar cells with graphene electrodes, Adv. Mater. 27(2015), 3632-3638. https://doi.org/10.1002/adma.201501145.
[159] Y. Zhong, L. Xu, C. Li, B. Zhang, W. Wu, Needle coke: A predominant carbon black alternative

for printable triple mesoscopic perovskite solar cells, Carbon 153 (2019) 602-608. https://doi.org/10.1016/j.carbon.2019.07.038.
[160] S. Liu, K. Cao, H. Li, J. Song, J. Han, Y. Shen, M. Wang, Full printable perovskite solar cells based on mesoscopic $TiO_2/Al_2O_3/NiO$ (carbon nanotubes) architecture, Solar Energy 144 (2017) 158-165. https://doi.org/10.1016/j.solener.2017.01.019.
[161] Q. Luo, H. Ma, F. Hao, Q. Hou, J. Ren, L. Wu, Z. Yao, Y. Zhou, N. Wang, K. Jiang, H. Lin, Z. Guo, 2017. Carbon nanotube based inverted flexible perovskite solar cells with all-inorganic charge contacts. Adv. Funct. Mater. 27, e1703068. https://doi.org/10.1002/adfm.201703068.
[162] C. Phillips, A. Al-Ahmadi, S.J. Potts, T. Claypole, D. Deganello, The effect of graphite and carbon black ratios on conductive ink performance, J. Mater. Sci. 52 (2017) 9520-9530. https://doi.org/10.1007/s10853-017-1114-6.
[163] L. Zhou, Y. Zuo, T.K. Mallick, S. Sundaram, 2019. Enhanced efficiency of carbon-based mesoscopic perovskite solar cells through a tungsten oxide nanoparticle additive in the carbon electrode. Sci. Rep. 9, e8778. https://doi.org/10.1038/s41598-019-45374-x.
[164] S. Bhandari, A. Roy, A. Ghosh, T.K. Mallick, S. Sundaram, Performance of WO_3-incorporated carbon electrodes for ambient mesoscopic perovskite solar cells, ACS Omega 5 (2020) 422-429. https://doi.org/10.1021/acsomega.9b02934.
[165] F.R. Li, Y. Xu, W. Chen, S.H. Xie, J.Y. Li, Nanotube enhanced carbon grids as top electrodes for fully printable mesoscopic semitransparent perovskite solar cells, J. Mater. Chem. A 5 (2017) 10374-10379. https://doi.org/10.1039/C7TA01383C.
[166] Z. Wei, K. Yan, H. Chen, Y. Yi, T. Zhang, X. Long, J. Li, L. Zhang, J. Wang, S. Yang, Cost-efficient clamping solar cells using candle soot for hole extraction from ambipolar perovskites, Energy Environ. Sci. 7 (2014) 3326-3333. https://doi.org/10.1039/C4EE01983K.
[167] L. Gao, Y. Zhou, F. Meng, Y. Li, A. Liu, Y. Li, C. Zhang, M. Fan, G. Wei, T. Ma, Several economical and eco-friendly bio-carbon electrodes for highly efficient perovskite solar cells, Carbon 162 (2020) 267-272. https://doi.org/10.1016/j.carbon.2020.02.049.
[168] Y. Yang, J. Xiao, H. Wei, L. Zhu, D. Li, Y. Luo, H. Wu, Q. Meng, An all-carbon counter electrode for highly efficient hole-conductor-free organo-metal perovskite solar cells, RSC Adv. 4 (2014) 52825-52830. https://doi.org/10.1039/C4RA09519G.
[169] H. Chen, Z. Wei, H. He, X. Zheng, K.S. Wong, S. Yang, 2016. Solvent engineering boosts the efficiency of paintable carbon-based perovskite solar cells to beyond 14%. Adv. Energy Mater. 6, e1502087. https://doi.org/10.1002/aenm.201502087.
[170] J. Ding, Y. Zhao, J. Duan, B. He, Q. Tang, Alloy-controlled work function for enhanced charge extraction in all-inorganic $CsPbBr_3$ perovskite solar cells, Chemsuschem 11 (2018) 1432-1437. https://doi.org/10.1002/cssc.201800060.
[171] Y. Zhang, X. Zhuang, K. Zhou, C. Cai, Z. Hu, J. Zhang, Y. Zhu, Vibration treated carbon electrode for highly efficient hole-conductor-free perovskite solar cells, Organic Electron. 52 (2018) 159-164. https://doi.org/10.1016/j.orgel.2017.10.018.
[172] Y. Wang, H. Zhao, Y. Mei, H. Liu, S. Wang, X. Li, Carbon nanotube bridging method for hole transport layer-free paintable carbon-based perovskite solar cells, ACS Appl. Mater. Interfaces 11 (2019) 916-923. https://doi.org/10.1021/acsami.8b18530.
[173] J. Kim, G. Lee, K. Lee, H. Yu, J.W. Lee, C.M. Yoon, S.G. Kim, S.K. Kim, J. Jang, Fluorine plasma treatment on carbon-based perovskite solar cells for rapid moisture protection layer formation and performance enhancement, Chem. Commun. 56 (2020) 535-538.

https://doi.org/10.1039/C9CC07785E.
[174] T. Liu, Z. Wang, L. Lou, S. Xiao, S. Zheng, S. Yang, 2020. Interfacial post-treatment for enhancing the performance of printable carbon‐based perovskite solar cells, Solar RRL 4, e1900278. https://doi.org/10.1002/solr.201900278.
[175] J. Yan, S. Lin, X. Qiu, H. Chen, K. Li, Y. Yuan, M. Long, B. Yang, Y. Gao, C. Zhou, 2019. Accelerated hole-extraction in carbon-electrode based planar perovskite solar cells by moisture-assisted post-annealing. Appl. Phys. Lett. 114, e103503. https://doi.org/10.1063/1.5087098.
[176] Q. Luo, H. Ma, Y. Zhang, X. Yin, Z. Yao, N. Wang, J. Li, S. Fan, K. Jiang, H. Lin, Cross-stacked superaligned carbon nanotube electrodes for efficient hole conductor-free perovskite solar cells, J. Mater. Chem. A 4 (2016) 5569-5577. https://doi.org/10.1039/C6TA01715K.
[177] J.W. Lee, I. Jeon, H.S. Lin, S. Seo, T.H. Han, A. Anisimov, E.I. Kauppinen, Y. Matsuo, S. Maruyama, Y. Yang, Vapor-assisted ex-situ doping of carbon nanotube toward efficient and stable perovskite solar cells, Nano Lett. 19 (2019) 2223-2230. https://doi.org/10.1021/acs.nanolett.8b04190.
[178] Q. Luo, H. Ma, Q. Hou, Y. Li, J. Ren, X. Dai, Z. Yao, Y. Zhou, L. Xiang, H. Du, H. He, N. Wang, K. Jiang, H. Lin, 2018. All-carbon-electrode-based endurable flexible perovskite solar cells. Adv. Funct. Mater. 28, e1706777. https://doi.org/10.1002/adfm.201706777.
[179] H. Su, J. Xiao, Q. Li, C. Peng, X. Zhang, C. Mao, Q. Yao, Y. Lu, Z. Ku, J. Zhong, W. Li, Y. Peng, F. Huang, Y. Cheng, 2020. Carbon film electrode based square-centimeter scale planar perovskite solar cells exceeding 17% efficiency. Mat. Sci. Semicon. Proc. 107, e104809. https://doi.org/10.1016/j.mssp.2019.104809.
[180] A.K. Baranwal, S. Kanaya, T.A.N. Peiris, G. Mizuta, T. Nishina, H. Kanda, T. Miyasaka, H. Segawa, S. Ito, 100 ºC thermal stability of printable perovskite solar cells using porous carbon counter electrodes, Chemsuschem 9 (2016) 2604-2608. https://doi.org/10.1002/cssc.201600933.
[181] Z. Liu, B. Sun, T. Shi, Z. Tang, G. Liao, Enhanced photovoltaic performance and stability of carbon counter electrode based perovskite solar cells encapsulated by PDMS, J. Mater. Chem. A 4 (2016) 10700-10709. https://doi.org/10.1039/C6TA02851A.
[182] W. Zhanhua, Z. Xiaoli, C. Haining, L. Xia, W. Zilong, Y. Shihe, A multifunctional C + epoxy/Ag-paint cathode enables efficient and stable operation of perovskite solar cells in watery environments, J. Mater. Chem. A 3 (2015) 16430-16434. https://doi.org/10.1039/C5TA03802B.
[183] S.G. Hashmi, A. Tiihonen, D. Martineau, M. Ozkan, P. Vivo, K. Kaunisto, V. Ulla, S.M. Zakeeruddin, M. Grätzel, Long term stability of air processed inkjet infiltrated carbon-based printed perovskite solar cells under intense ultra-violet light soaking, J. Mater. Chem. A 5 (2017) 4797-14802. https://doi.org/10.1039/C6TA10605F.
[184] Z. Fu, M. Xu, Y. Sheng, Z. Yan, J. Meng, C. Tong, D. Li, Z. Wan, Y. Ming, A. Mei, Y. Hu, Y. Rong, H. Han, 2019. Encapsulation of printable mesoscopic perovskite solar cells enables high temperature and long‐term outdoor stability. Adv. Funct. Mater. 29, e1809129. https://doi.org/10.1002/adfm.201809129.